Supporting Information

Christoph Kreitner[a,b], *and Katja Heinze*[a,*]

[a] Institute of Inorganic and Analytical Chemistry, Johannes Gutenberg-University of Mainz,

Duesbergweg 10-14, 55128 Mainz, Germany

[b] Graduate School Materials Science in Mainz, Staudingerweg 9, 55128 Mainz, Germany

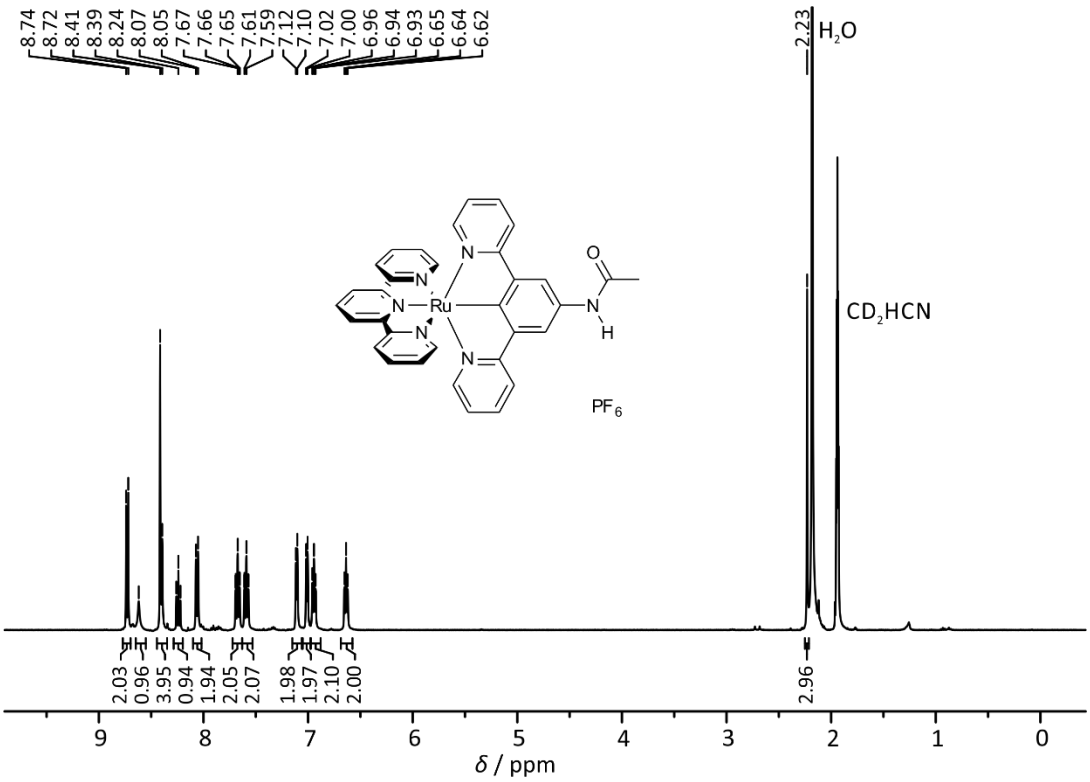

Figure S1 ^{1}H NMR spectrum (400 MHz) of **1**(PF_6) in CD_3CN.

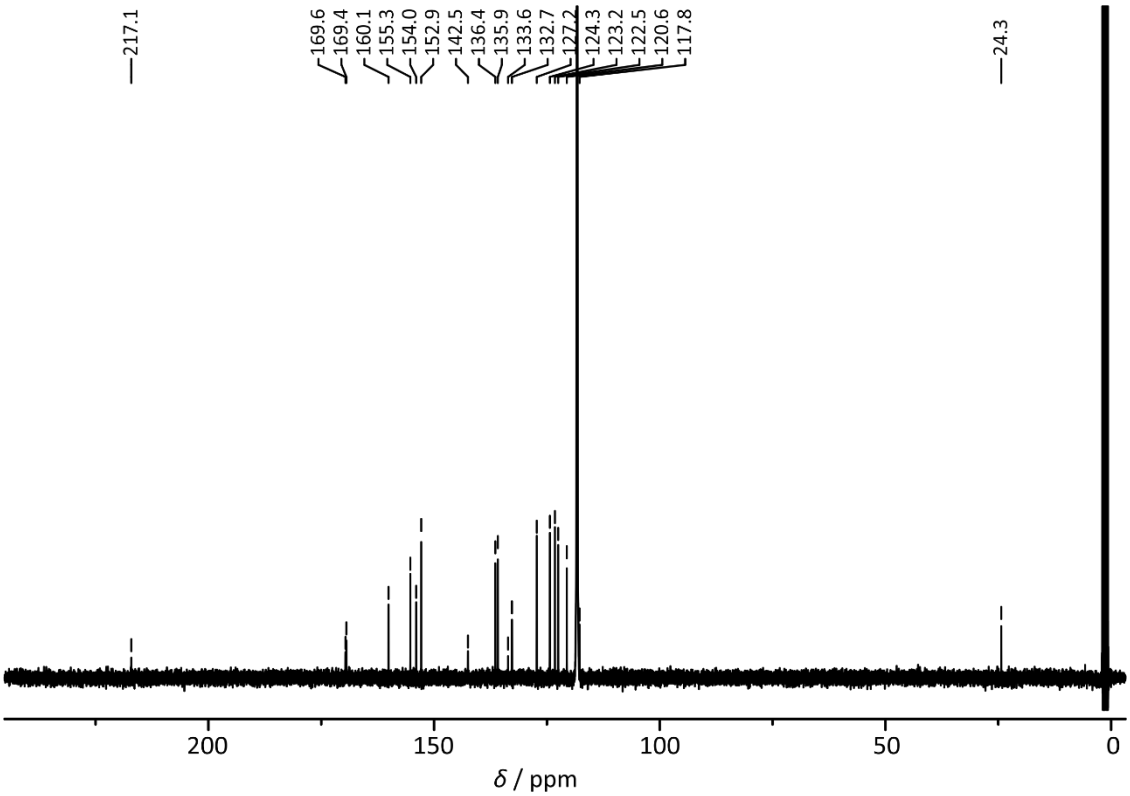

Figure S2 ^{13}C NMR spectrum (100 MHz) of **1**(PF_6) in CD_3CN.

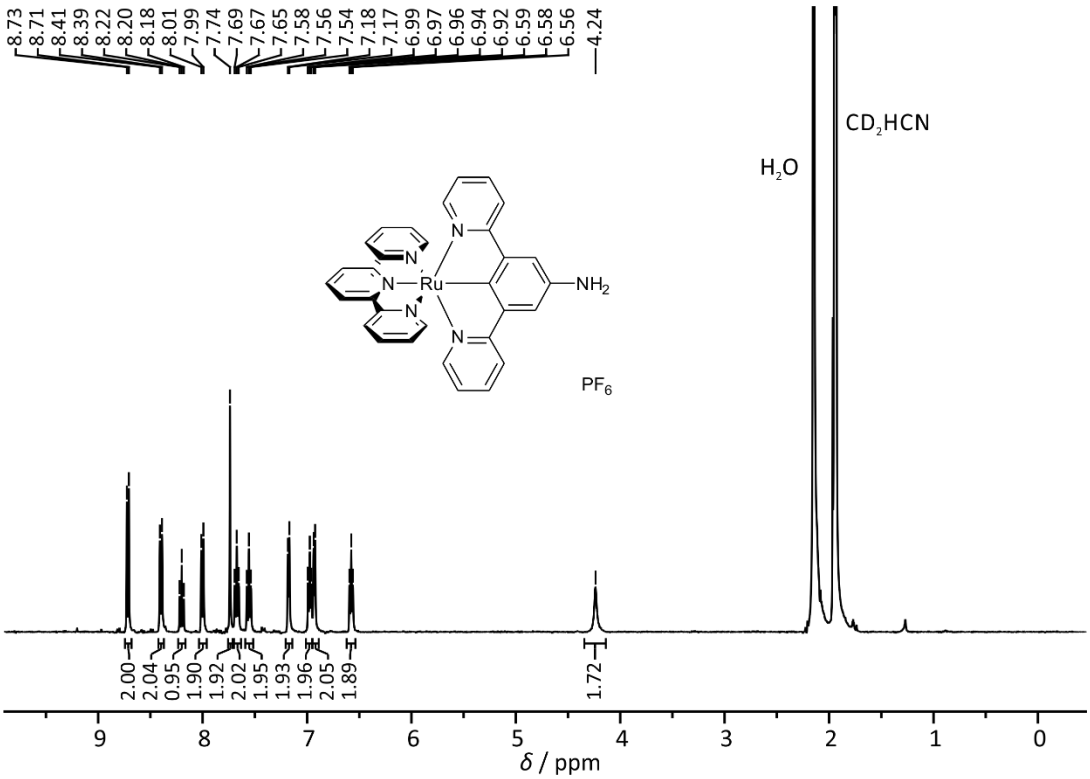

Figure S3 ^{1}H NMR spectrum (400 MHz) of **2**(PF_6) in CD_3CN.

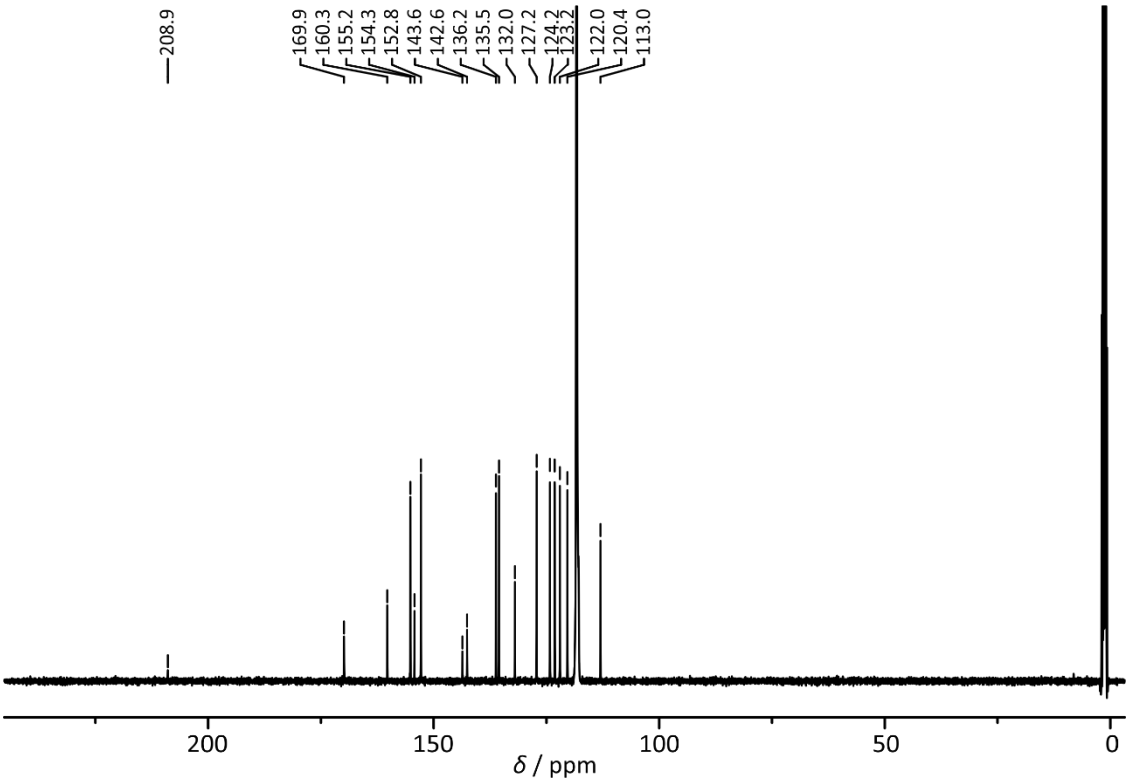

Figure S4 ^{13}C NMR spectrum (100 MHz) of **2**(PF_6) in CD_3CN.

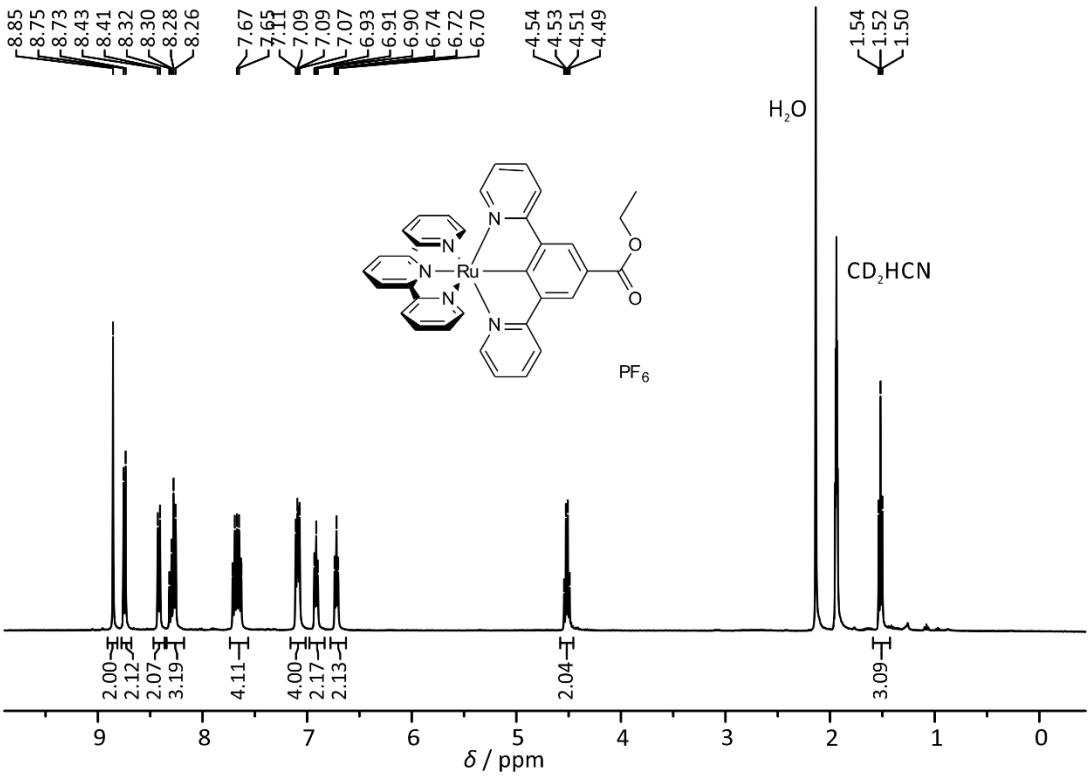

Figure S5 ^{1}H NMR spectrum (400 MHz) of **3**(PF_6) in CD_3CN.

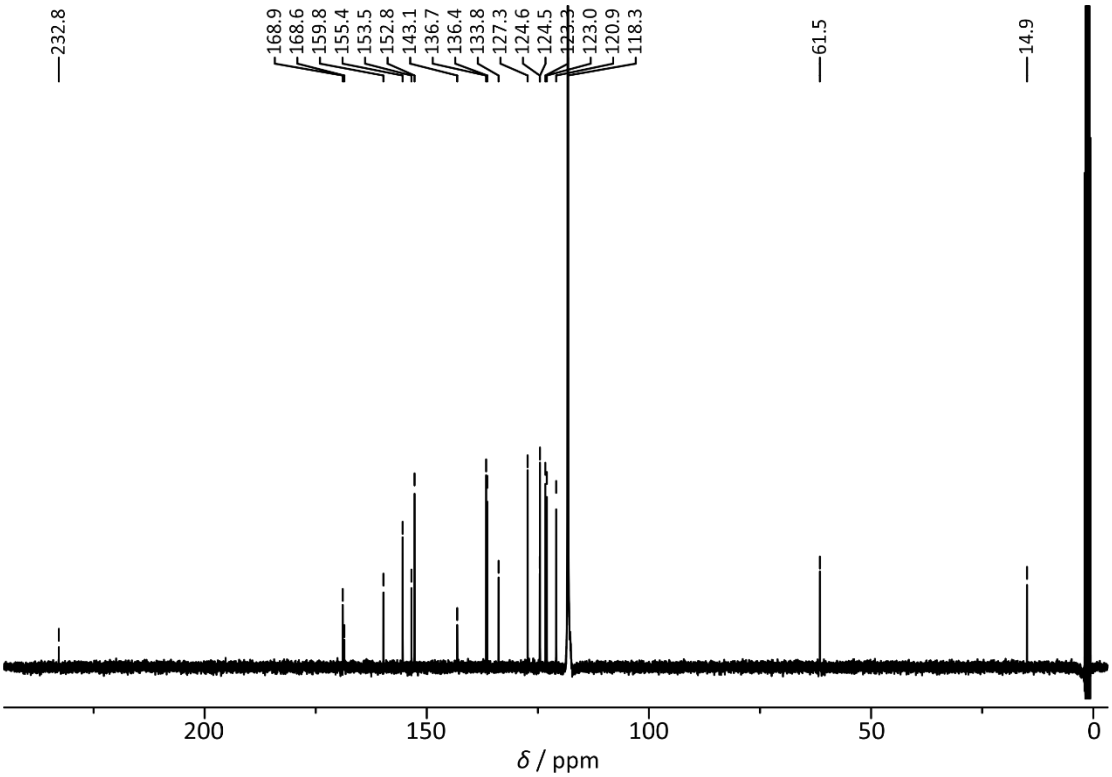

Figure S6 ^{13}C NMR spectrum (100 MHz) of **3**(PF_6) in CD_3CN.

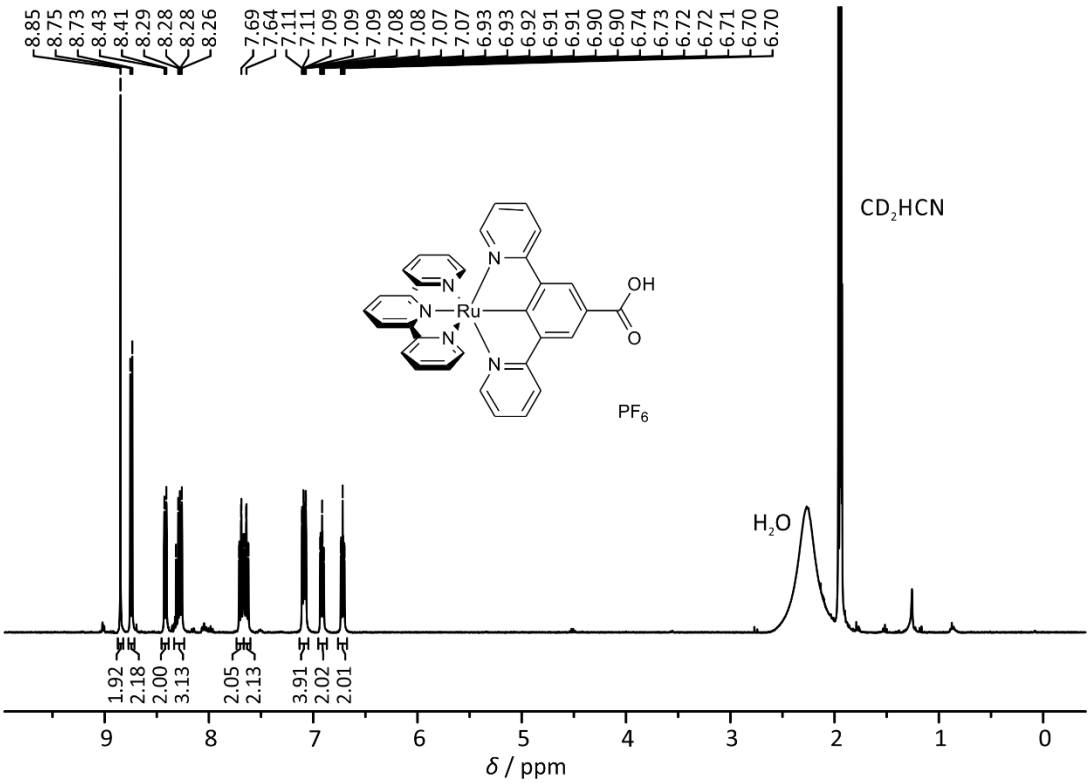

Figure S7 ^{1}H NMR spectrum (400 MHz) of **4**(PF_6) in CD_3CN.

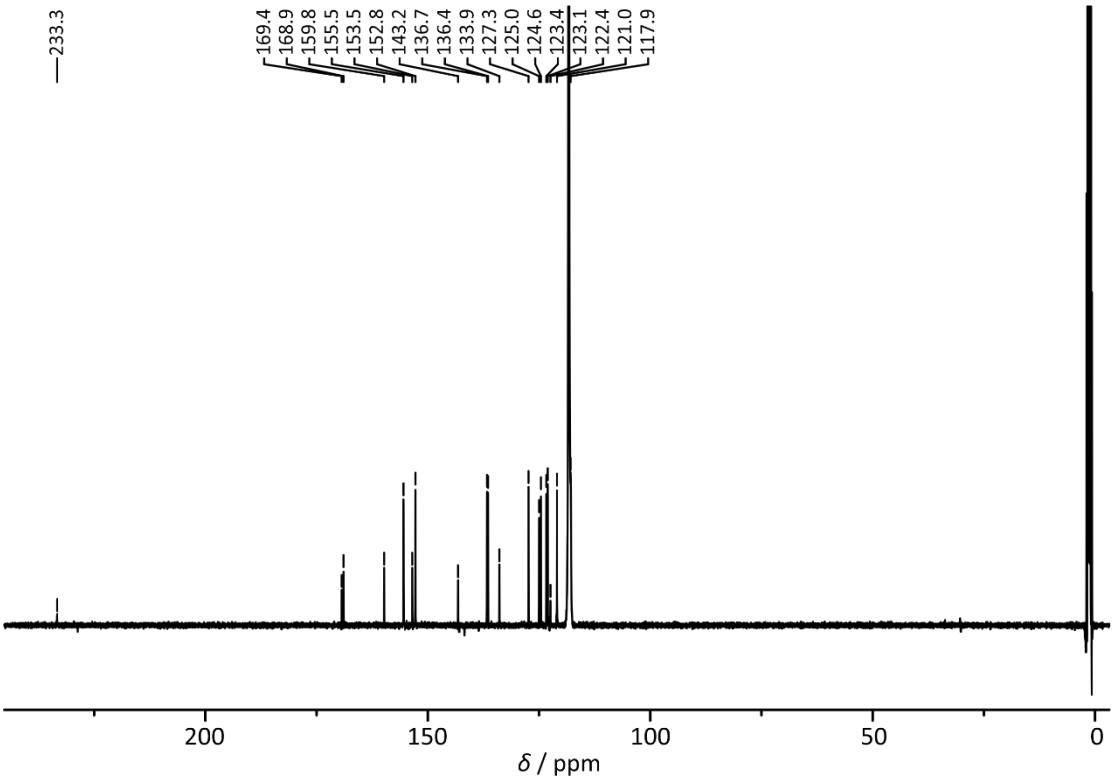

Figure S8 ^{13}C NMR spectrum (100 MHz) of **4**(PF_6) in CD_3CN.

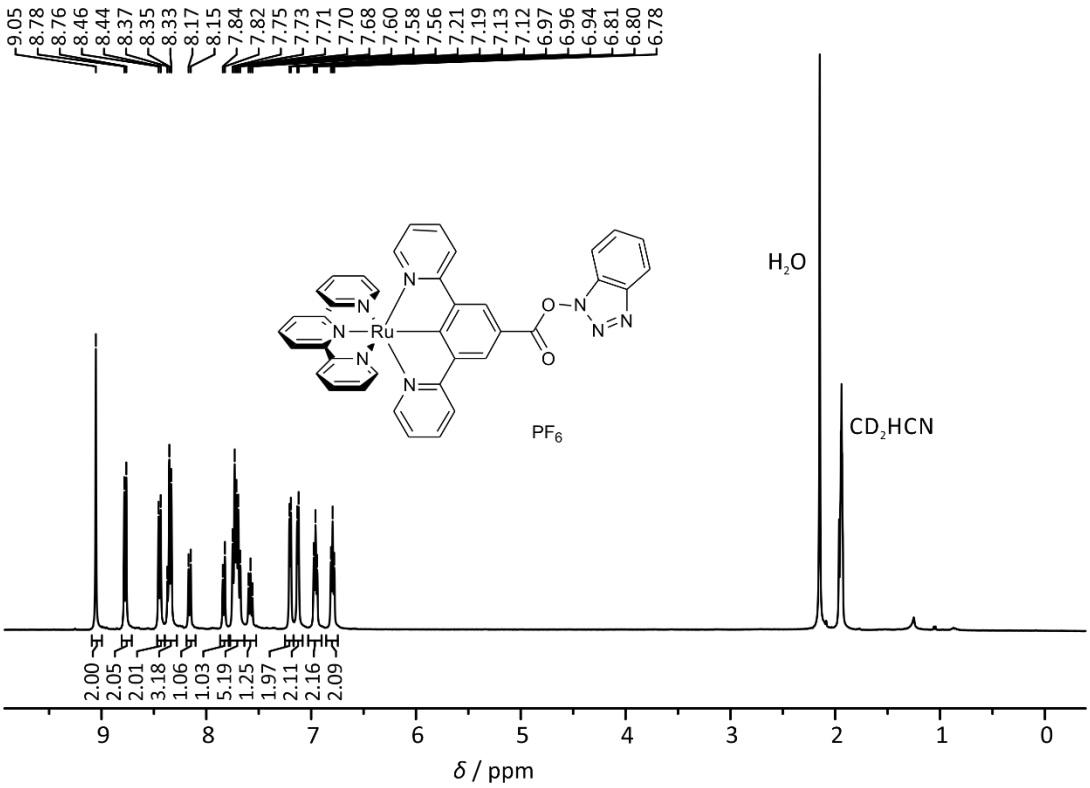

Figure S9 ^{1}H NMR spectrum (400 MHz) of **5**(PF_6) in CD_3CN.

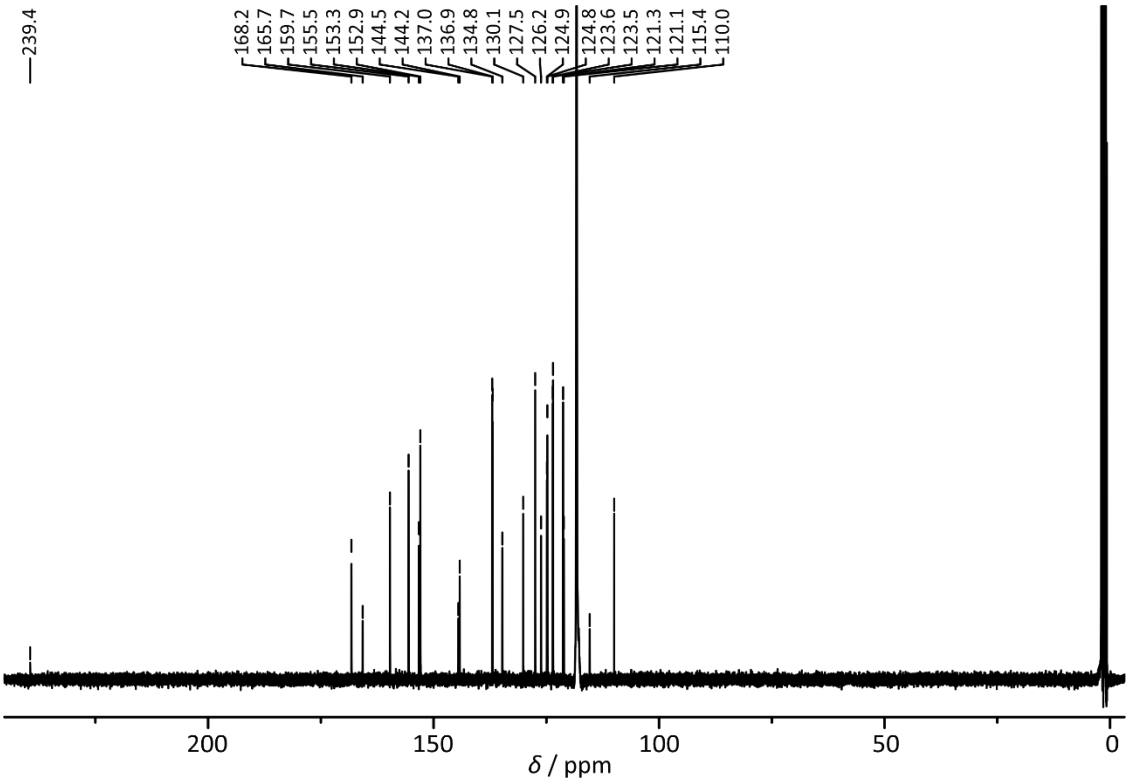

Figure S10 ^{13}C NMR spectrum (100 MHz) of **5**(PF_6) in CD_3CN.

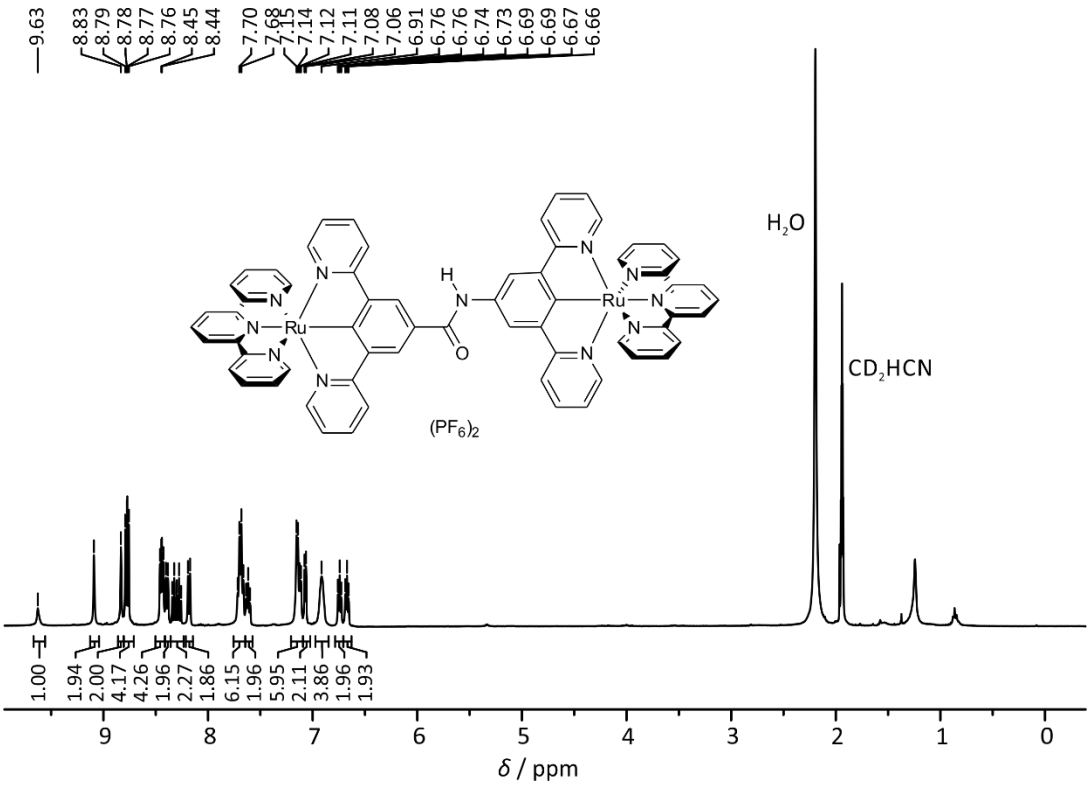

Figure S11 ^{1}H NMR spectrum (400 MHz) of **6**(PF_6) in CD_3CN.

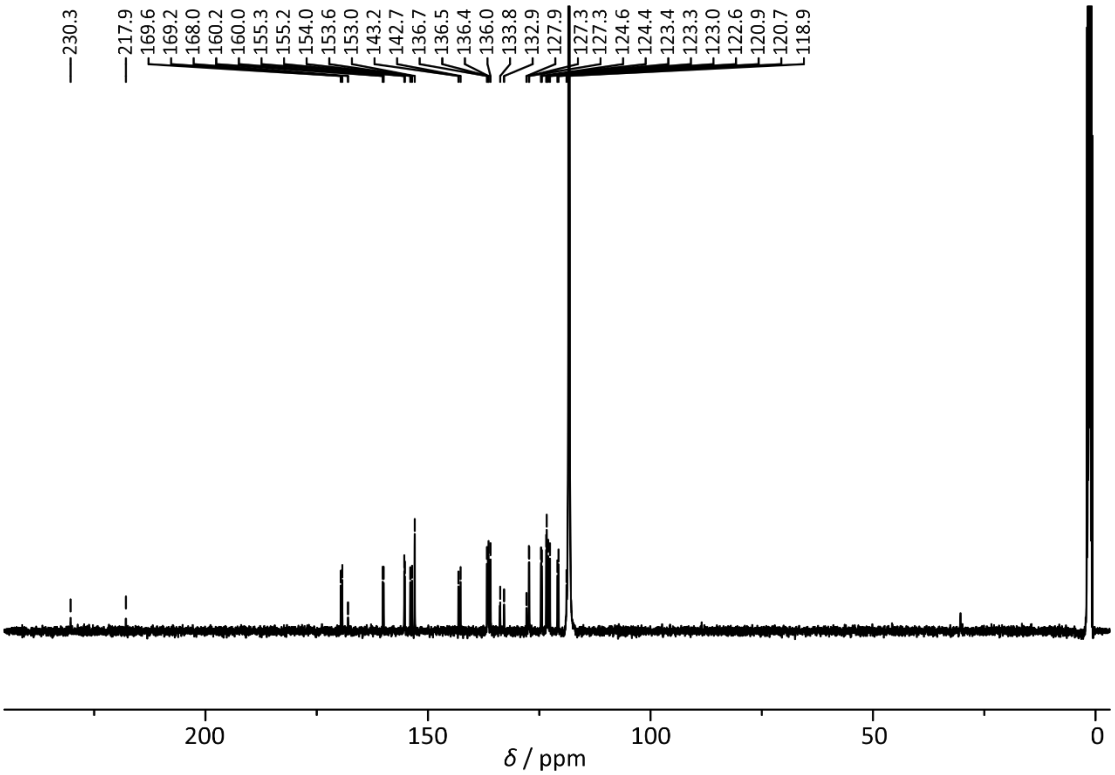

Figure S12 ^{13}C NMR spectrum (100 MHz) of **6**(PF_6) in CD_3CN.

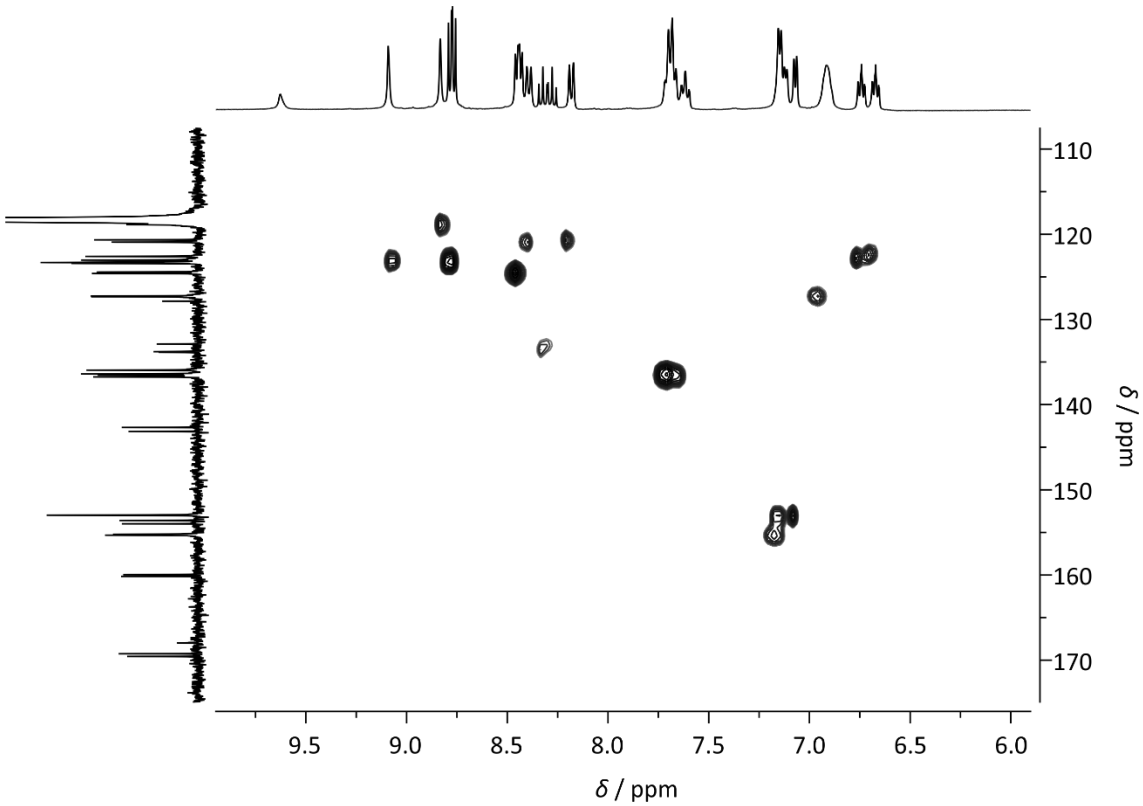

Figure S13 Aromatic region of the ^{1}H-^{13}C HSQC NMR spectrum of **6**(PF_6) in CD_3CN.

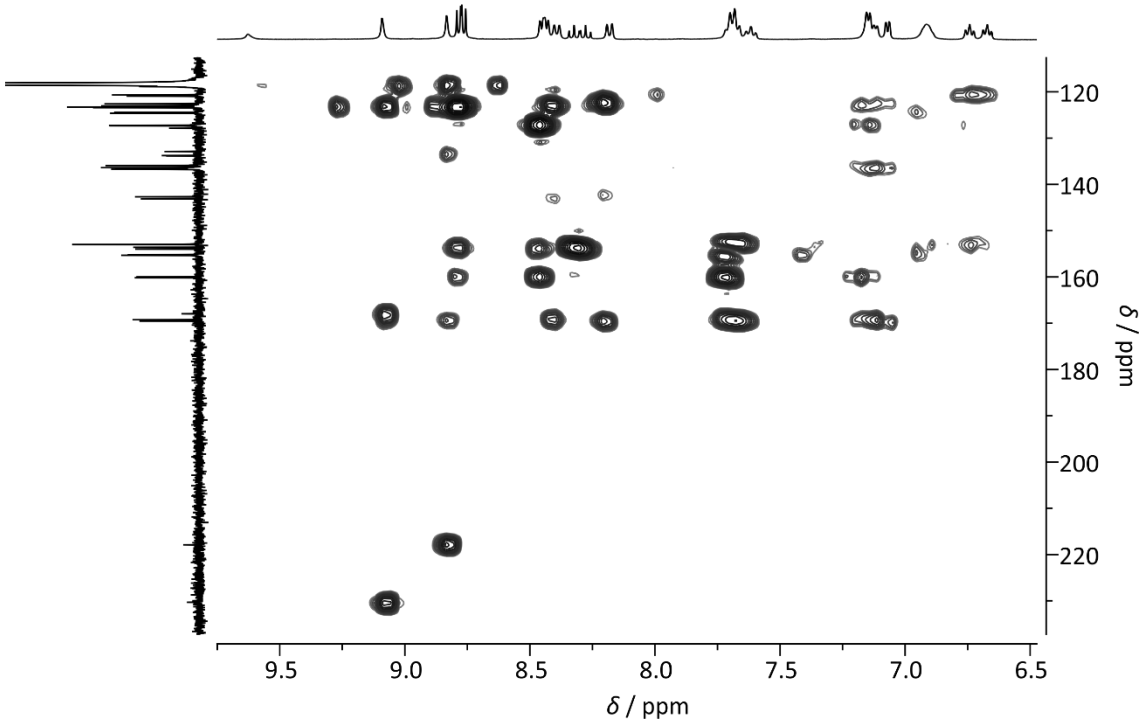

Figure S14 Aromatic region of the ^{1}H-^{13}C HMBC NMR spectrum of **6**(PF_6) in CD_3CN.

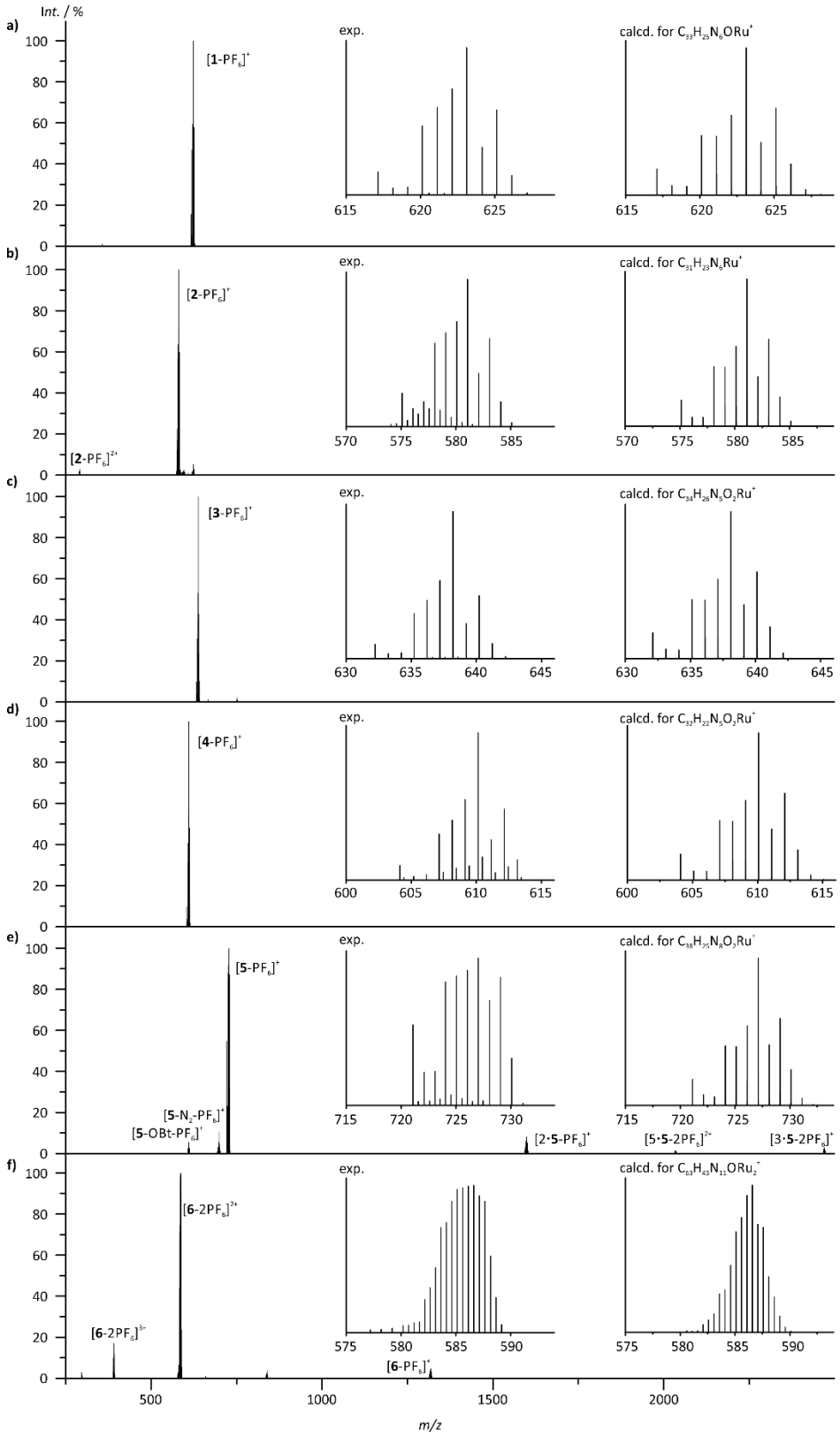

Figure S15 ESI mass spectra of **a) 1**(PF_6), **b) 2**(PF_6), **c) 3**(PF_6), **d) 4**(PF_6), **e) 5**(PF_6), and **f) 6**(PF_6) in CH_3CN. Insets show experimental and calculated isotope pattern of the most intense peak.

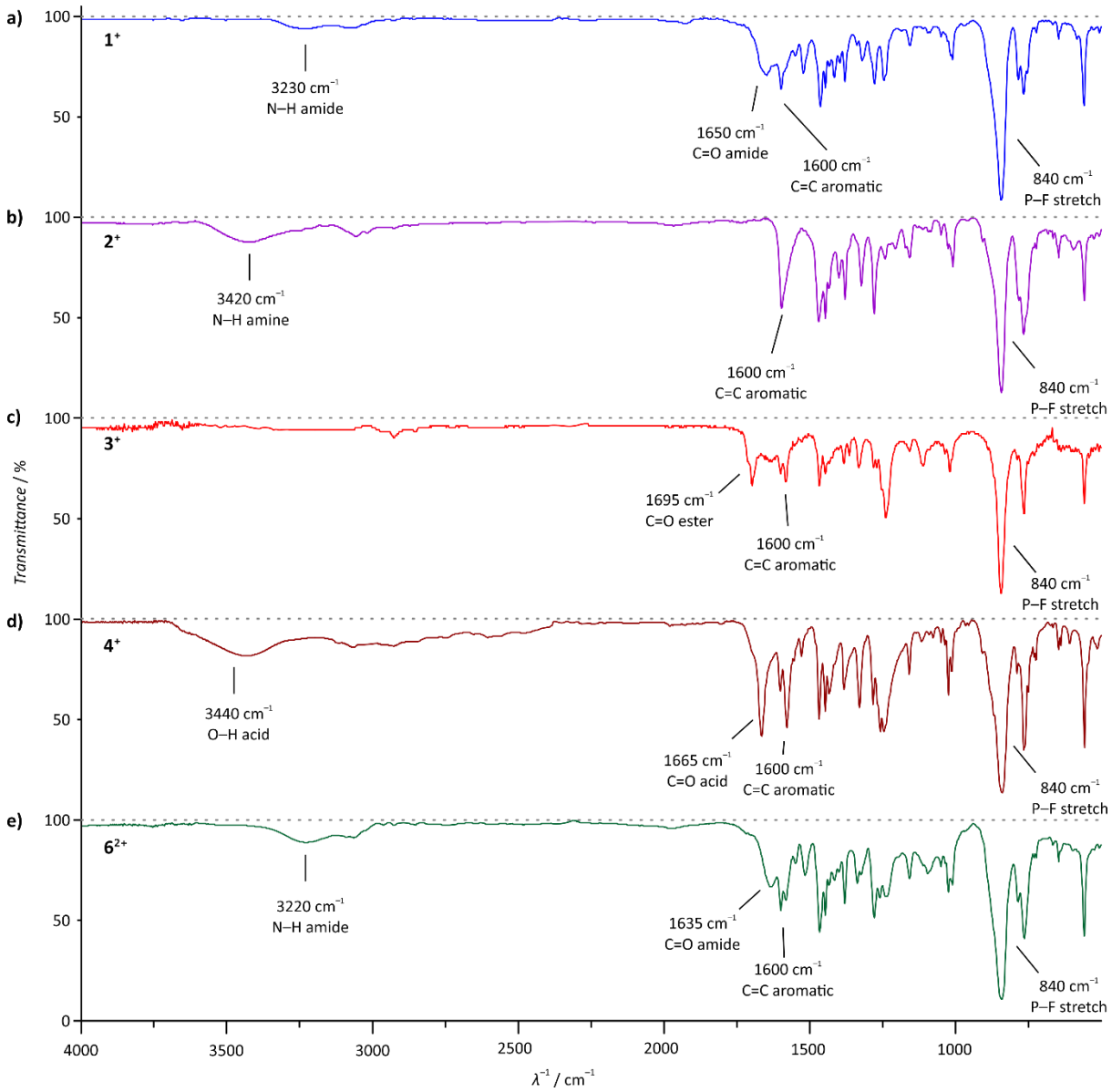

Figure S16 IR spectra of complexes **a)** **1**(PF_6), **b)** **2**(PF_6), **c)** **3**(PF_6), **d)** **4**(PF_6) and **e)** **6**$(PF_6)_2$ in the solid state (KBr disk).

Table S1 Selected molecular orbitals of **1**$^+$, **2**$^+$, **3**$^+$, and **4**$^+$ (B3LYP, def2-SV(P), ZORA, COSMO(acetonitrile)) including orbital number (energy *E* in eV) (contour value 0.07). Hydrogen atoms are omitted for clarity.

	1$^+$	**2**$^+$	**3**$^+$	**4**$^+$
LUMO+3	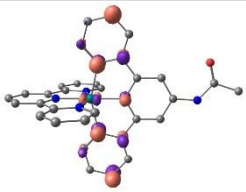 MO162 (−1.50)	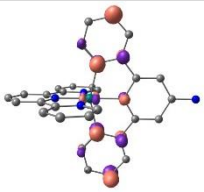 MO151 (−1.45)	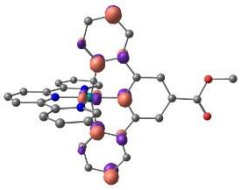 MO162 (−1.57)	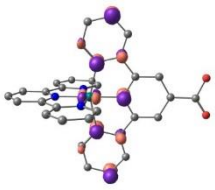 MO158 (−1.58)
LUMO+2	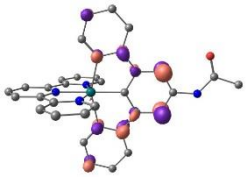 MO161 (−1.82)	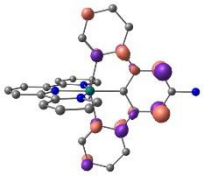 MO150 (−1.74)	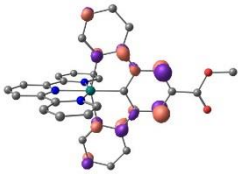 MO161 (−1.86)	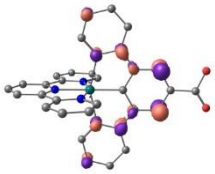 MO157 (−1.87)
LUMO+1	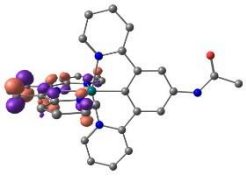 MO160 (−2.23)	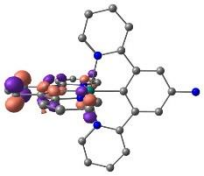 MO149 (−2.20)	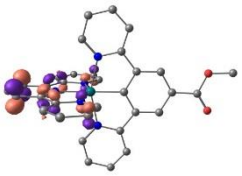 MO160 (−2.27)	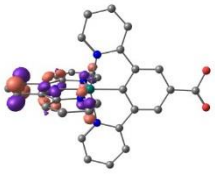 MO156 (−2.28)
LUMO	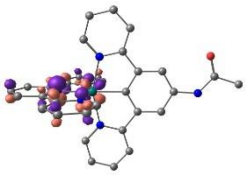 MO159 (−2.27)	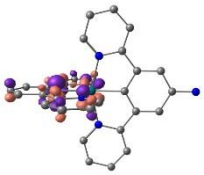 MO148 (−2.23)	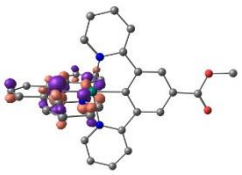 MO159 (−2.33)	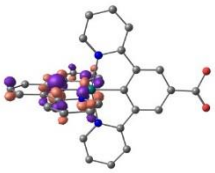 MO155 (−2.34)
HOMO	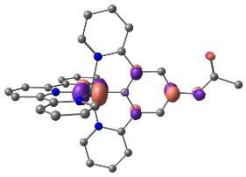 MO158 (−4.99)	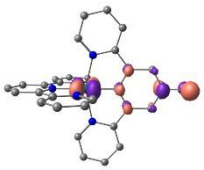 MO147 (−4.71)	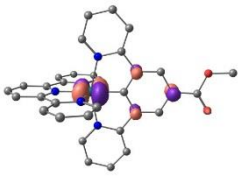 MO158 (−5.31)	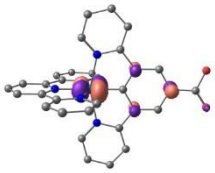 MO154 (−5.33)
HOMO-1	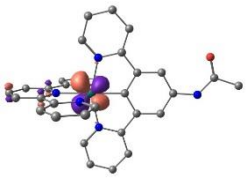 MO157 (−5.35)	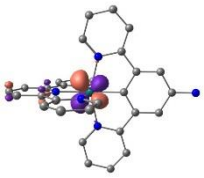 MO146 (−5.27)	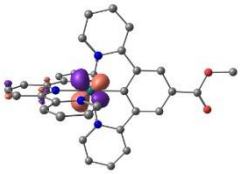 MO157 (−5.47)	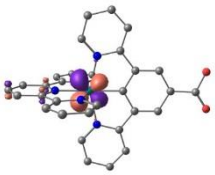 MO153 (−5.48)
HOMO-2	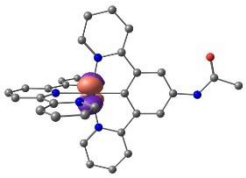 MO156 (−5.43)	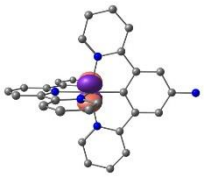 MO145 (−5.36)	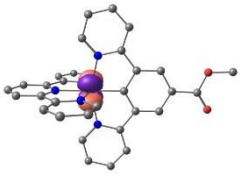 MO156 (−5.52)	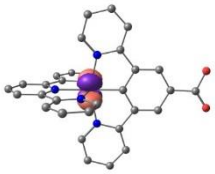 MO152 (−5.53)

Table S2 DFT calculated spin densities of complexes **1**$^{+}$ – **4**$^{+}$ after single and double oxidation as well as single and double reduction (B3LYP, def2-SV(P), ZORA, COSMO(acetonitrile); contour value: 0.01).

charge	**2+**	**3+**	**0**	**1−**
1	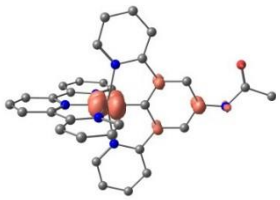	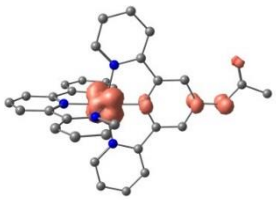	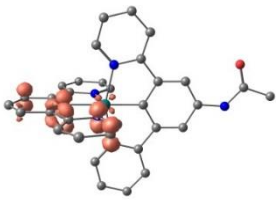	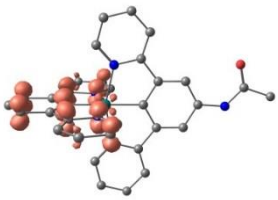
2	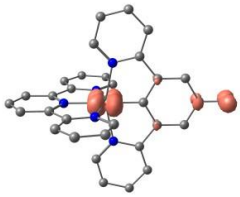	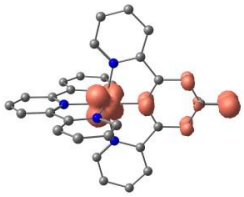	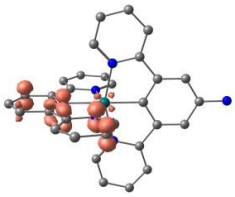	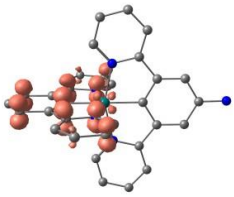
3	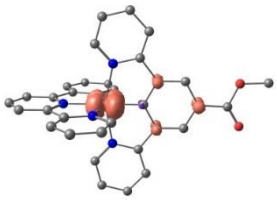	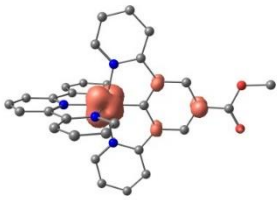	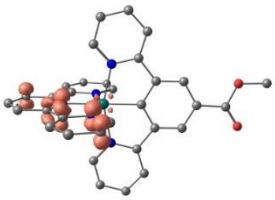	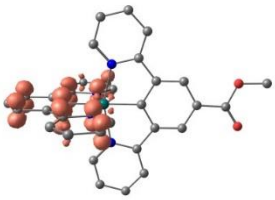
4	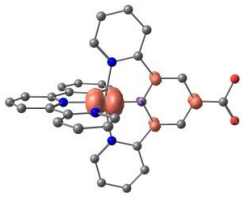	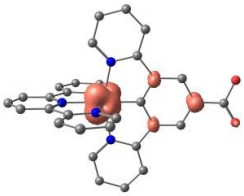	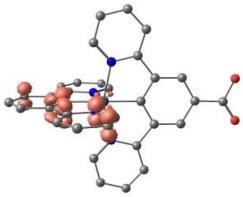	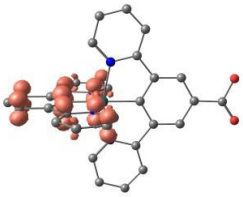

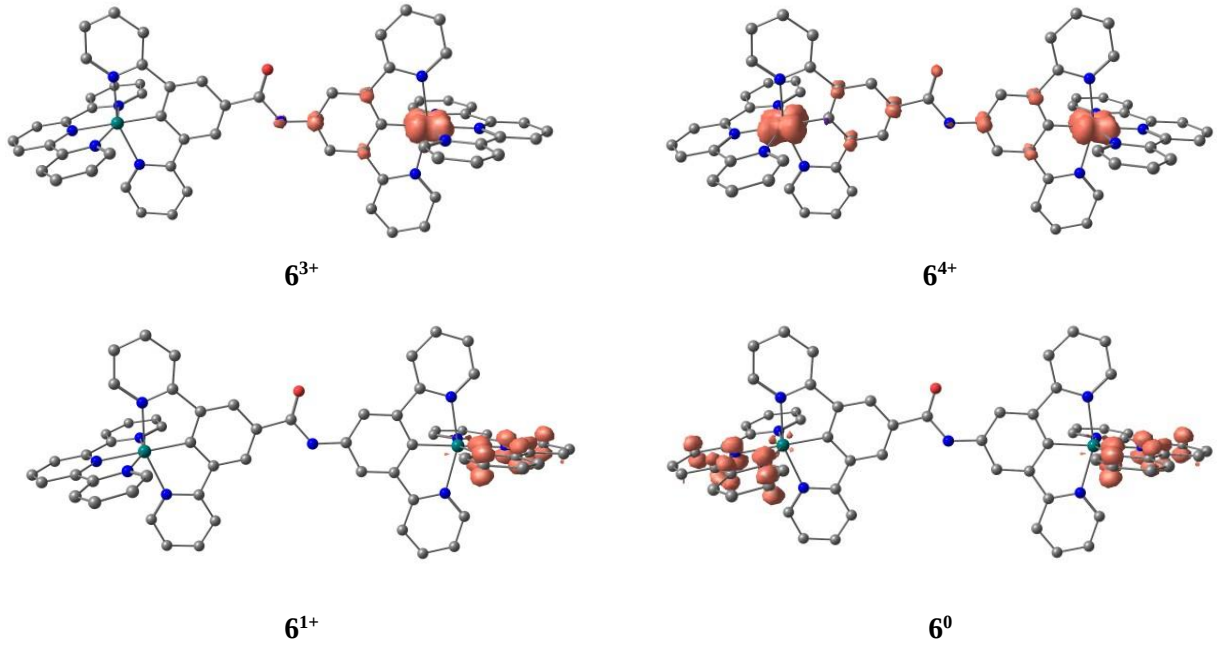

Figure S17 DFT calculated spin densities of the singly and doubly oxidized complexes **6**$^{3+}$ and **6**$^{4+}$ as well as the singly and doubly reduced complexes **6**$^{+}$ and **6**^{0} (B3LYP, def2-SV(P), ZORA, COSMO(acetonitrile); contour value: 0.01).

Table S3 Selected molecular orbitals of **6**$^{2+}$ (B3LYP, def2-SV(P), ZORA, COSMO(acetonitrile)) including orbital number (energy *E* in eV) (contour value 0.07). Hydrogen atoms are omitted for clarity.

LUMO+7	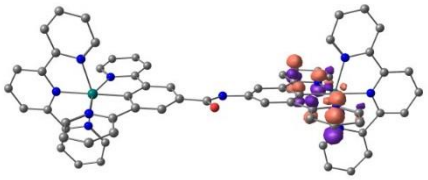 MO304 (−1.54)	**LUMO**	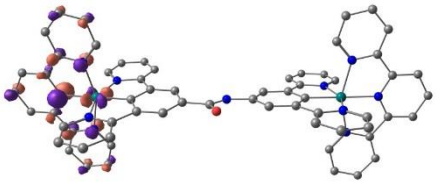 MO297 (−2.36)
LUMO+6	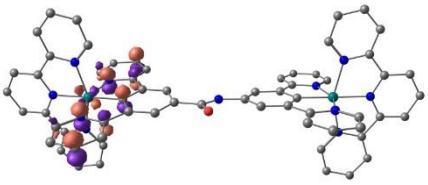 MO303 (−1.61)	**HOMO**	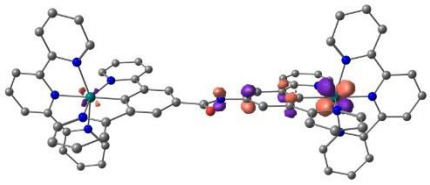 MO296 (−5.00)
LUMO+5	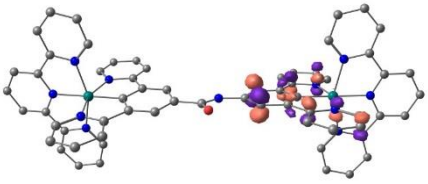 MO302 (−1.86)	**HOMO-1**	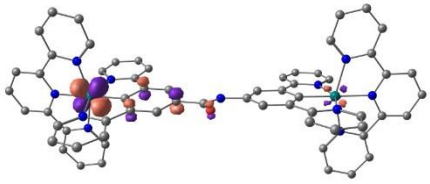 MO295 (−5.36)

LUMO+4	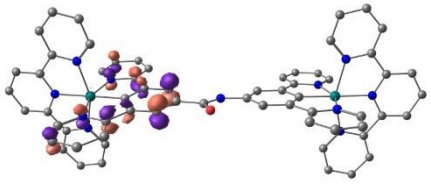 MO301 (−1.92)	**HOMO-2**	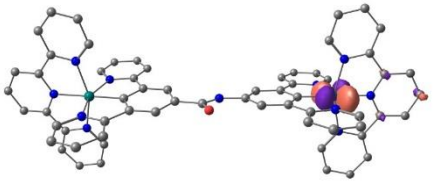 MO294 (−5.39)
LUMO+3	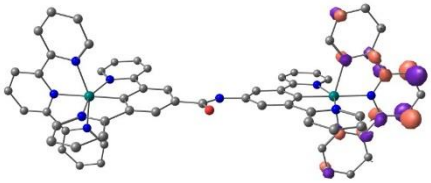 MO300 (−2.26)	**HOMO-3**	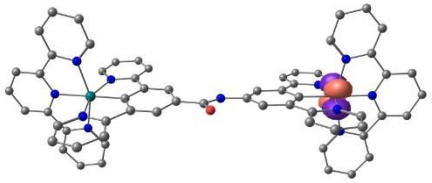 MO293 (−5.46)
LUMO+2	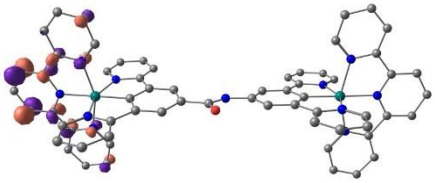 MO299 (−2.31)	**HOMO-4**	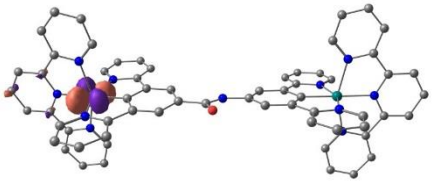 MO292 (−5.49)
LUMO+1	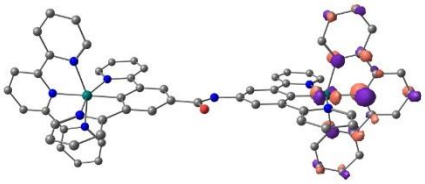 MO298 (−2.31)	**HOMO-5**	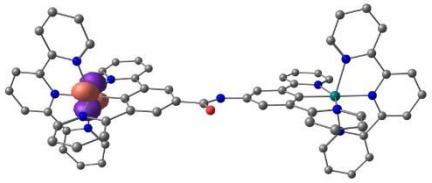 MO291 (−5.55)

Table S4 Selected vertical TD-DFT transitions of **1**$^+$ (B3LYP, def2-SV(P), ZORA, COSMO(acetonitrile)) sorted by their energy including difference density plots $|\Psi_{ES}|^2 - |\Psi_{GS}|^2$ (contour value 0.005, purple: depletion, orange: gain in electron density). Hydrogen atoms are omitted for clarity.

	$\tilde{\upsilon}$ / cm^{-1}	λ / nm	f_{osc}	$\lvert\Psi_{ES}\rvert^2 - \lvert\Psi_{GS}\rvert^2$		$\tilde{\upsilon}$ / cm^{-1}	λ / nm	f_{osc}	$\lvert\Psi_{ES}\rvert^2 - \lvert\Psi_{GS}\rvert^2$
1	13967	716	$4.30 \cdot 10^{-8}$	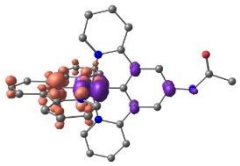	**10**	22891	437	0.00001	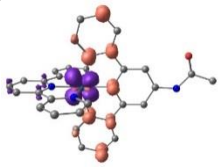
2	14972	668	0.00066	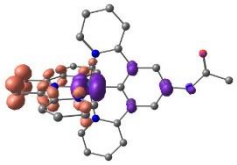	**13**	24853	402	0.09267	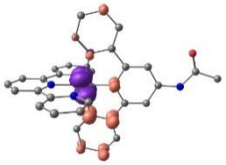
3	17170	582	0.00723	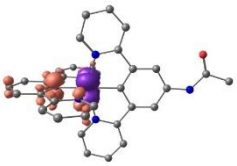	**14**	25051	399	0.03568	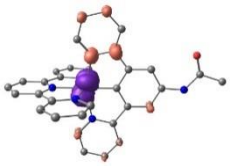

4	18458	542	0.00512	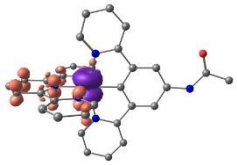	**19**	28073	356	0.03405	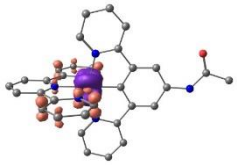
5	18728	534	0.05845	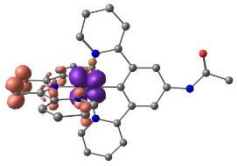	**20**	28080	356	0.03646	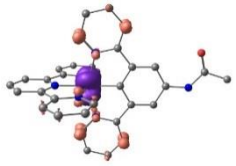
6	20594	486	0.09011	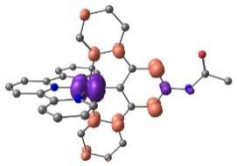	**21**	28236	354	0.03297	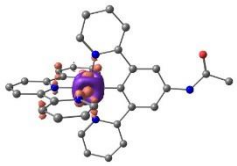
7	21029	476	0.00695	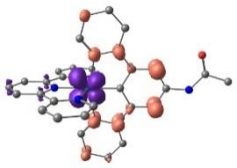	**23**	28339	353	0.04613	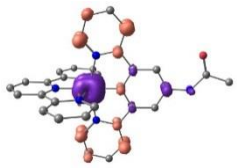
8	21890	457	0.14519	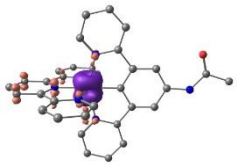	**33**	32361	309	0.01697	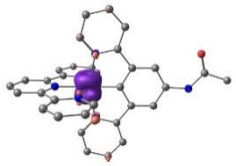
9	22432	446	0.01191	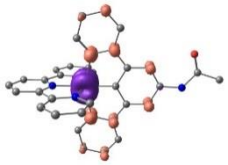	**34**	32565	307	0.02433	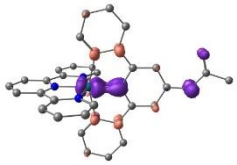

Table S5 Selected vertical TD-DFT transitions of **2**$^{+}$ (B3LYP, def2-SV(P), ZORA, COSMO(acetonitrile)) sorted by their energy including difference density plots $|\Psi_{ES}|^2 - |\Psi_{GS}|^2$ (contour value 0.005, purple: depletion, orange: gain in electron density). Hydrogen atoms are omitted for clarity.

	$\tilde{\upsilon}$ / cm^{-1}	λ / nm	f_{osc}	$\lvert\Psi_{ES}\rvert^2 - \lvert\Psi_{GS}\rvert^2$		$\tilde{\upsilon}$ / cm^{-1}	λ / nm	f_{osc}	$\lvert\Psi_{ES}\rvert^2 - \lvert\Psi_{GS}\rvert^2$
1	12179	821	$4.57 \cdot 10^{-7}$	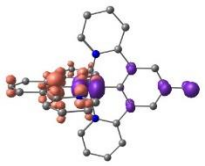	**15**	24593	407	0.02282	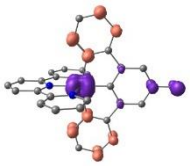
2	12929	773	0.00062	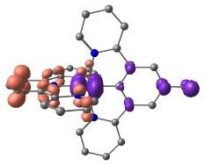	**14**	24780	404	0.10567	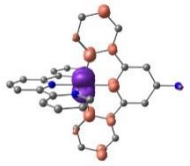

3	16901	592	0.00626	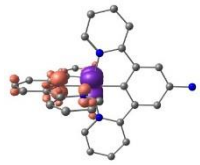	**18**	26283	381	0.01072	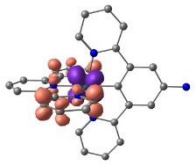
4	18183	550	0.00412	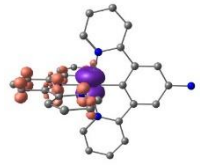	**23**	27516	363	0.07089	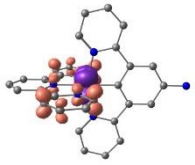
5	18431	543	0.06130	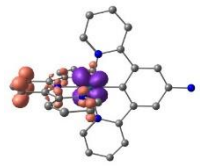	**24**	28019	357	0.06192	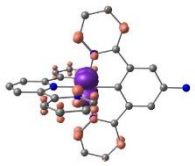
6	19735	507	0.11450	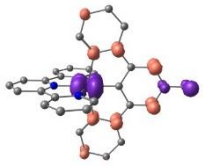	**29**	30082	332	0.01847	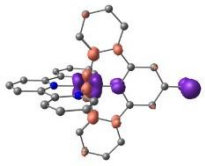
7	20703	483	0.05125	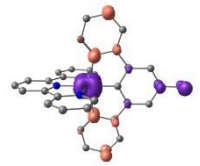	**32**	31177	321	0.01062	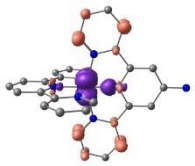
8	20931	478	0.00062	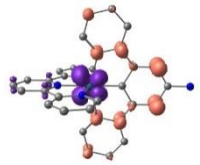	**36**	32993	303	0.03505	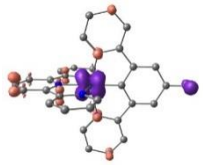
9	21795	459	0.03127	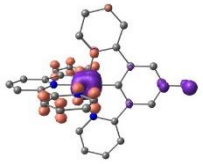	**46**	33168	302	0.02112	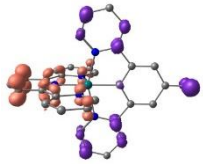
10	22232	450	0.06565	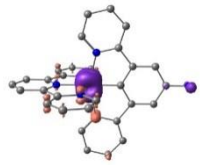					

Table S6 Selected vertical TD-DFT transitions of **3**$^+$ (B3LYP, def2-SV(P), ZORA, COSMO(acetonitrile)) sorted by their energy including difference density plots $|\Psi_{ES}|^2 - |\Psi_{GS}|^2$ (contour value 0.005, purple: depletion, orange: gain in electron density). Hydrogen atoms are omitted for clarity.

$\tilde{\upsilon}$ / cm^{-1}	λ / nm	f_{osc}	$\|\Psi_{ES}\|^2 - \|\Psi_{GS}\|^2$	$\tilde{\upsilon}$ / cm^{-1}	λ / nm	f_{osc}	$\|\Psi_{ES}\|^2 - \|\Psi_{GS}\|^2$

1	15881	630	$1.75 \cdot 10^{-6}$	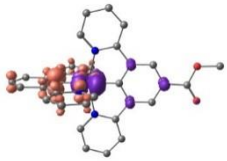	**10**	23117	433	$2.95 \cdot 10^{-7}$	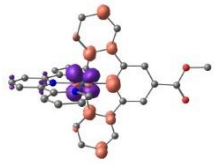
3	17096	585	0.00062	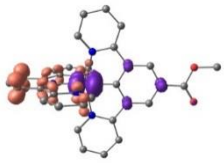	**9**	23166	432	0.00512	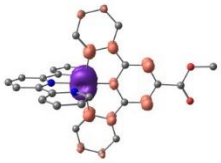
2	17563	569	0.00902	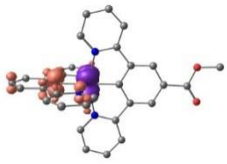	**11**	24728	404	0.10876	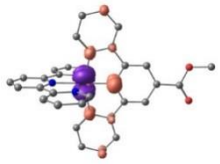
4	18873	530	0.00626	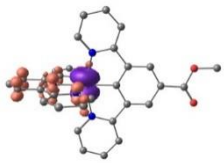	**18**	28165	355	0.05247	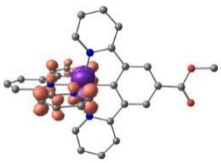
5	19215	520	0.05380	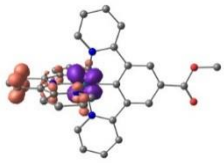	**19**	28534	351	0.08369	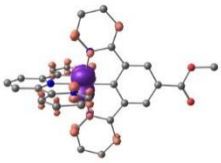
8	21496	465	0.00058	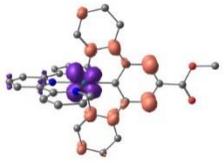	**24**	29891	335	0.11957	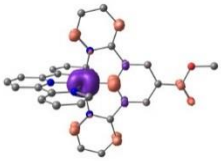
6	21914	456	0.06001	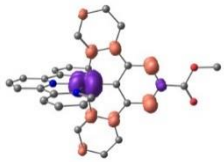	**26**	30040	333	0.03531	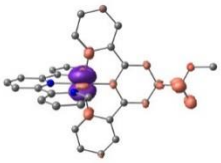
7	22283	449	0.17235	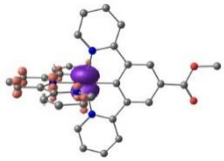	**28**	30815	325	0.05395	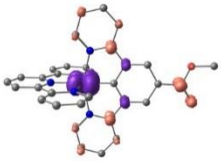

Table S7 Selected vertical TD-DFT transitions of **4**$^+$ (B3LYP, def2-SV(P), ZORA, COSMO(acetonitrile)) sorted by their energy including difference density plots $|\Psi_{ES}|^2 - |\Psi_{GS}|^2$ (contour value 0.005, purple: depletion, orange: gain in electron density). Hydrogen atoms are omitted for clarity.

$\tilde{\upsilon}$ / cm^{-1}	λ / nm	f_{osc}	$\|\Psi_{ES}\|^2 - \|\Psi_{GS}\|^2$	$\tilde{\upsilon}$ / cm^{-1}	λ / nm	f_{osc}	$\|\Psi_{ES}\|^2 - \|\Psi_{GS}\|^2$

1	15985	626	$3.06 \cdot 10^{-6}$	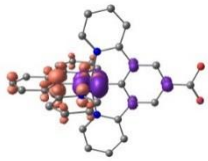	**10**	23117	433	$1.66 \cdot 10^{-6}$	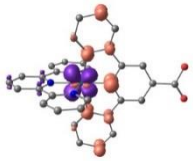
3	17210	581	0.00063	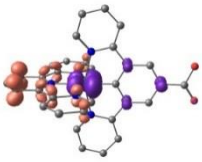	**9**	23179	431	0.00662	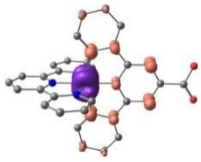
2	17603	568	0.00919	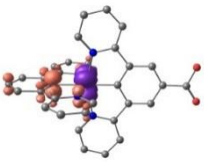	**11**	24694	405	0.10794	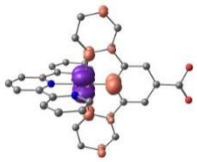
4	18916	529	0.00616	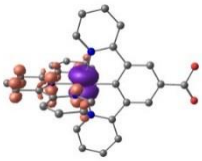	**18**	28199	355	0.05170	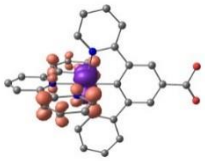
5	19264	519	0.05350	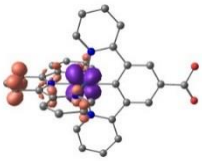	**19**	28564	350	0.08182	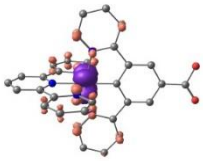
8	21518	465	0.00191	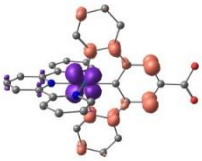	**26**	29633	338	0.04010	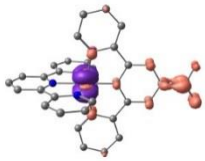
6	21948	456	0.05880	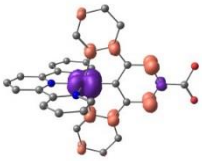	**24**	29888	335	0.12162	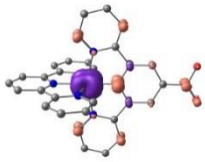
7	22325	448	0.16638	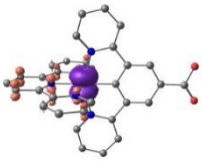	**28**	30892	324	0.03754	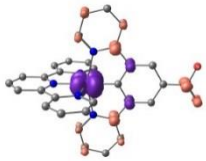

Table S8 Selected vertical TD-DFT transitions of $\mathbf{6}^{2+}$ (B3LYP, def2-SV(P), ZORA, COSMO(acetonitrile)) sorted by their energy including difference density plots $|\Psi_{ES}|^2 - |\Psi_{GS}|^2$ (contour value 0.005, purple: depletion, orange: gain in electron density). Hydrogen atoms are omitted for clarity.

	$\tilde{\upsilon}$ / cm^{-1}	λ / nm	f_{osc}	$\lvert\Psi_{ES}\rvert^2 - \lvert\Psi_{GS}\rvert^2$

1	13941	717	$2.65 \cdot 10^{-6}$
3	14926	670	0.00063
2	15509	645	$5.04 \cdot 10^{-6}$
12	15932	628	0.00149
21	16101	621	$4.49 \cdot 10^{-6}$
25	16358	611	$1.44 \cdot 10^{-6}$
6	16487	607	0.00070
19	16676	600	$2.95 \cdot 10^{-6}$
26	16800	595	$3.25 \cdot 10^{-7}$
23	16842	594	0.00013

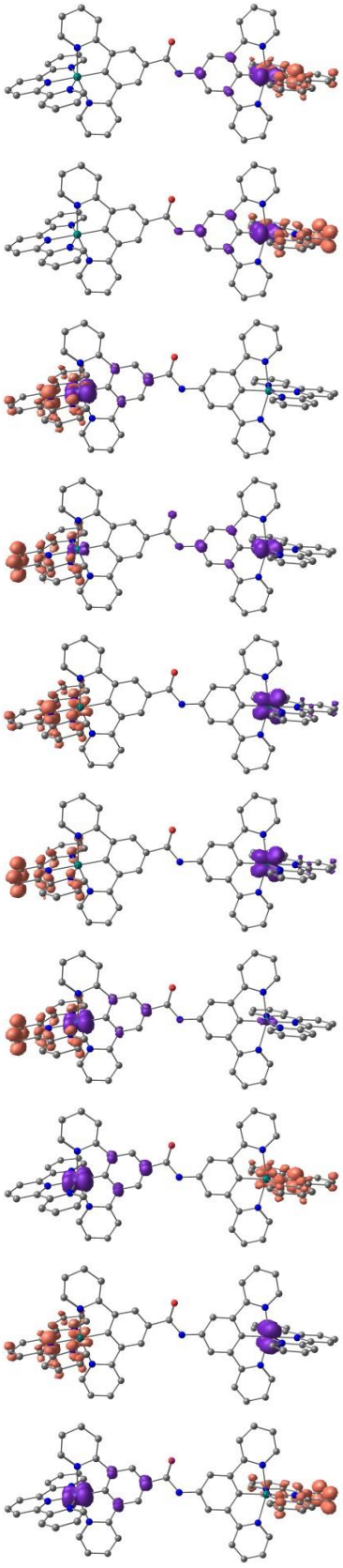

11	17953	557	0.02374
10	18348	545	0.02801
7	18491	541	0.00986
9	18780	533	0.05506
8	18854	530	0.01090
13	20498	488	0.07937
14	20813	481	0.05640
22	21003	476	0.00912
15	21806	459	0.34875
18	22284	449	0.13827

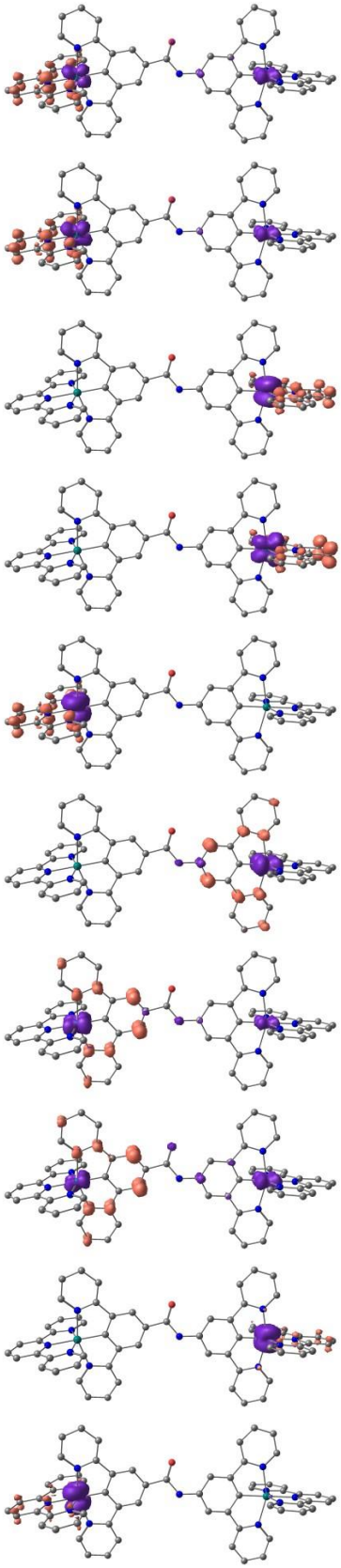

41	22291	449	0.01702
20	22393	447	0.00896
36	24755	404	0.04056
38	24977	400	0.16626
44	25891	386	0.03412
50	26642	375	0.01756

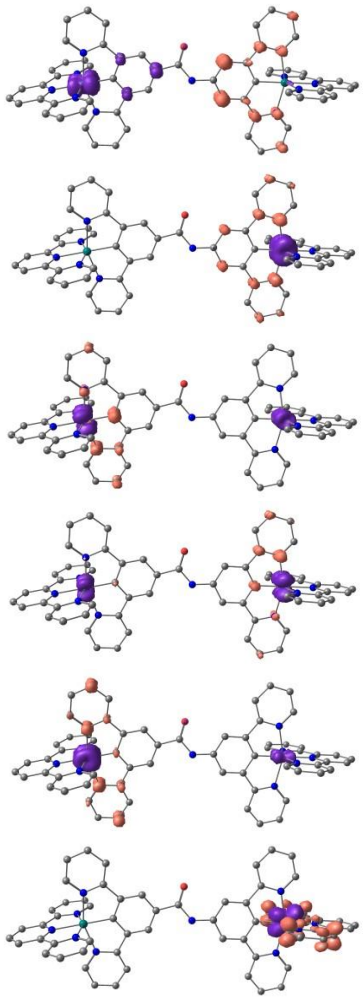

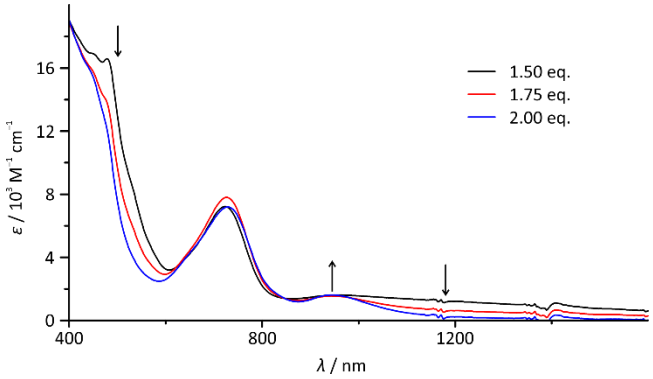

Figure S18 Absorption spectra of $\mathbf{6}^{2+}$ after addition of 1.50, 1.75 and 2.00 equivalents of $(NH_4)_2[Ce(NO_3)_6]$ as oxidant ($\mathbf{6}^{3+}\rightarrow\mathbf{6}^{4+}$).

Table S9 Selected vertical TD-DFT transitions of **6**$^{3+}$ (B3LYP, def2-SV(P), ZORA, COSMO(acetonitrile)) sorted by their energy including difference density plots $|\Psi_{ES}|^2 - |\Psi_{GS}|^2$ (contour value 0.005, purple: depletion, orange: gain in electron density). Hydrogen atoms are omitted for clarity.

	$\tilde{\nu}$ / cm^{-1}	λ / nm	f_{osc}	$\lvert\Psi_{ES}\rvert^2 - \lvert\Psi_{GS}\rvert^2$
1	4255	2350	$4.63 \cdot 10^{-7}$	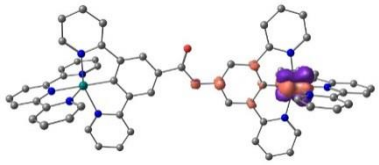
2	4495	2225	0.00026	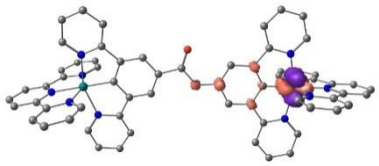
3	7172	1394	0.06523	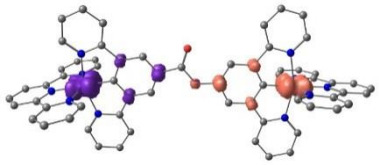
4	8319	1202	$2.50 \cdot 10^{-6}$	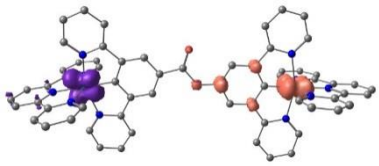
5	8674	1153	0.00050	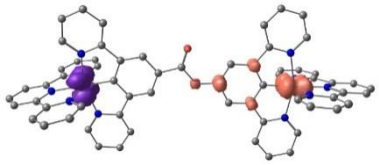
11	13059	766	0.00423	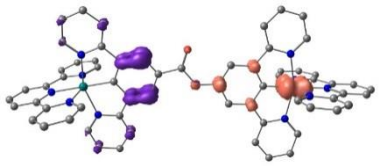
6	14873	672	0.00036	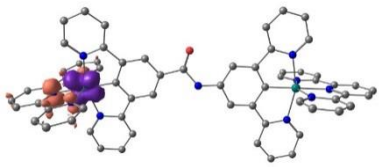
9	15530	644	$8.00 \cdot 10^{-8}$	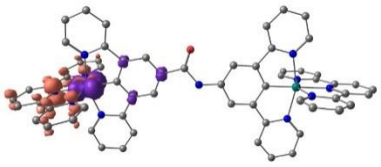
7	15758	635	0.19415	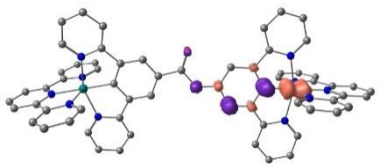

8	15988	626	0.04104
10	16361	611	$5.85 \cdot 10^{-6}$
19	17520	571	0.00070
13	17850	560	0.00943
44	17998	556	0.01475
37	18303	546	0.01029
21	19180	521	0.01038
24	19526	512	0.05026
25	19889	503	0.00272
30	20522	487	0.00723

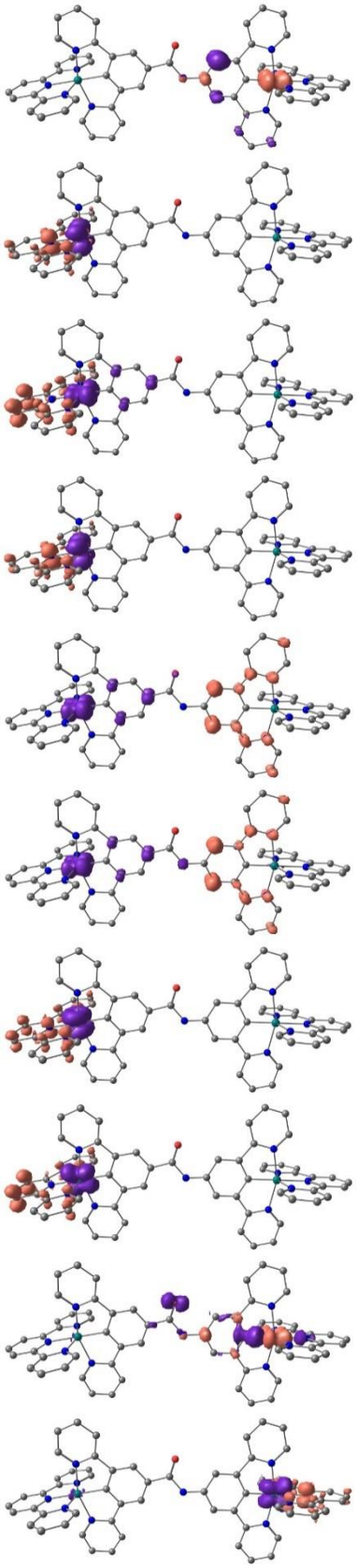

35	20717	483	0.00345
31	20725	483	0.00114
42	21775	459	0.05831
43	22161	451	0.20749
49	22512	444	0.01892
48	22618	442	0.07026

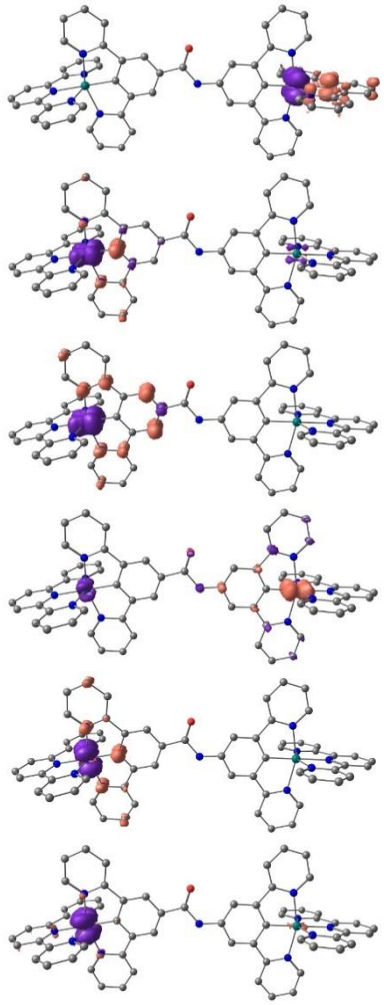

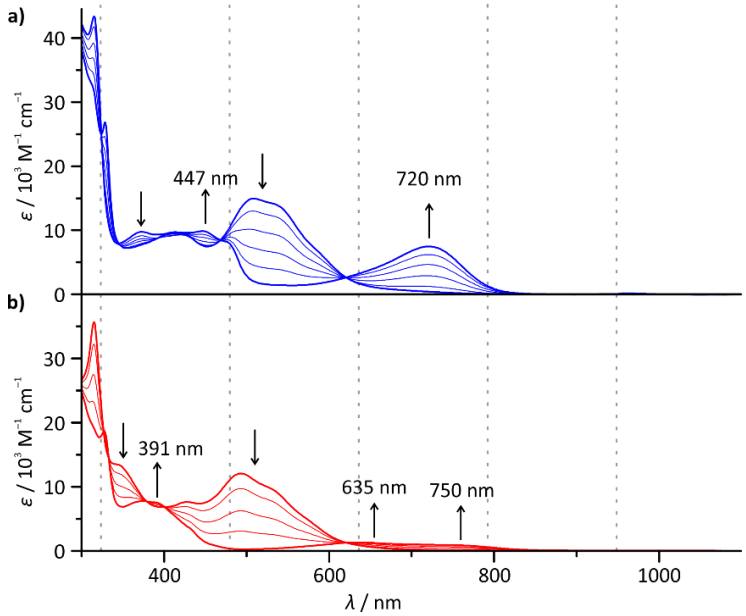

Figure S19 UV-Vis absorption spectra of $\mathbf{1}^+$ (top, blue) and $\mathbf{3}^+$ (bottom, red) in dry acetonitrile upon addition of 0→1 equivalents of $(NH_4)_2[Ce(NO_3)_6]$ as oxidant.

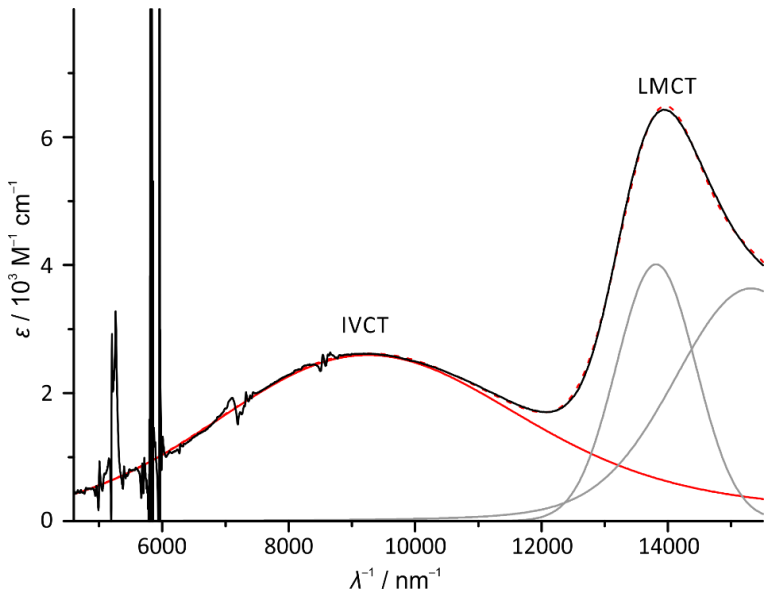

Figure S20 Fit of the IVCT band of $\mathbf{6}^{3+}$ (generated in situ by oxidation of $\mathbf{6}^{2+}$ with one equivalent of $(NH_4)_2[Ce(NO_3)_6]$ in acetonitrile). The figure shows the experimental spectrum (black), the fit of the spectral range between 3500 and 16000 cm^{-1} (red, dashed), the band fits of the LMCT bands (grey) and the fit of the IVCT band (red).

Fit parameters:

IVCT:

$\tilde{\nu}_{max}$ = 8585 cm^{-1}

ε_{max} = 2600 M^{-1} cm^{-1}

$\tilde{\nu}_{1/2}$ = 6020 cm^{-1}

LMCT 1:

$\tilde{\nu}_{max}$ = 13780 cm^{-1}

ε_{max} = 4010 M^{-1} cm^{-1}

$\tilde{\nu}_{1/2}$ = 1480 cm^{-1}

LMCT 2:

$\tilde{\nu}_{max}$ = 15225 cm^{-1}

ε_{max} = 3640 M^{-1} cm^{-1}

$\tilde{\nu}_{1/2}$ = 2900 cm^{-1}

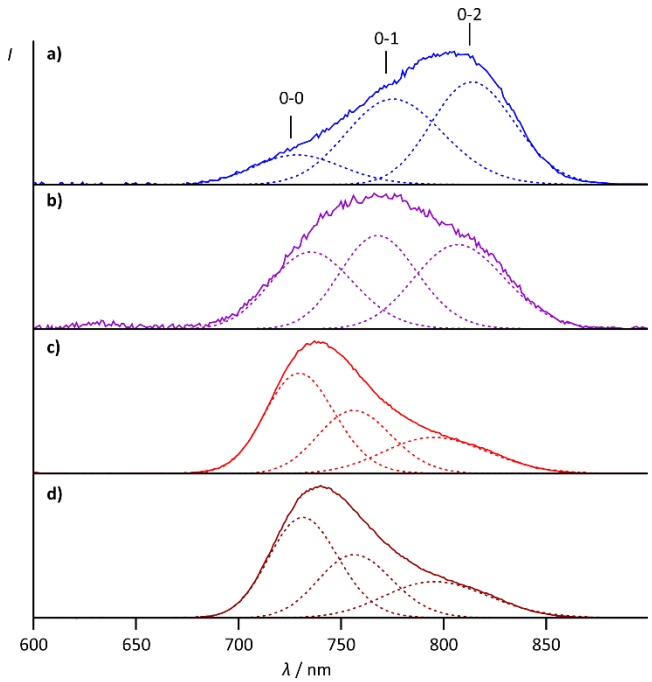

Figure S21 Spectral decomposition of the emission spectra of **a) 1**$^+$ **b) 2**$^+$ **c) 3**$^+$ and **d) 4**$^+$ (recorded at 155 K in butyronitrile solution) into individual gaussians. Vibrational progression energies are 740 cm^{-1} (**1**$^+$), 710 cm^{-1} (**2**$^+$) and 670 cm^{-1} (**3**$^+$ and **4**$^+$).[1,2]

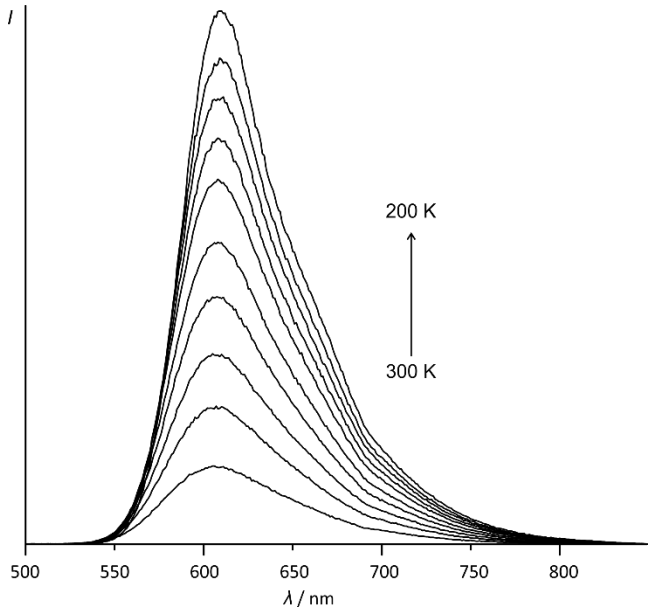

Figure S22 Emission spectra of $[Ru(bpy)_3](PF_6)_2$ in butyronitrile in the temperature range between 300 K and 200 K.

---

[1] Z. Murtaza, D. K. Graff, A. P. Zipp, L. A. Worl, Jones, Wayne E. Jr., W. D. Bates and T. J. Meyer, *J. Phys. Chem.*, 1994, **98**, 10504–10513.

[2] K. Heinze, K. Hempel and M. Beckmann, *Eur. J. Inorg. Chem.*, 2006, **2006**, 2040–2050.

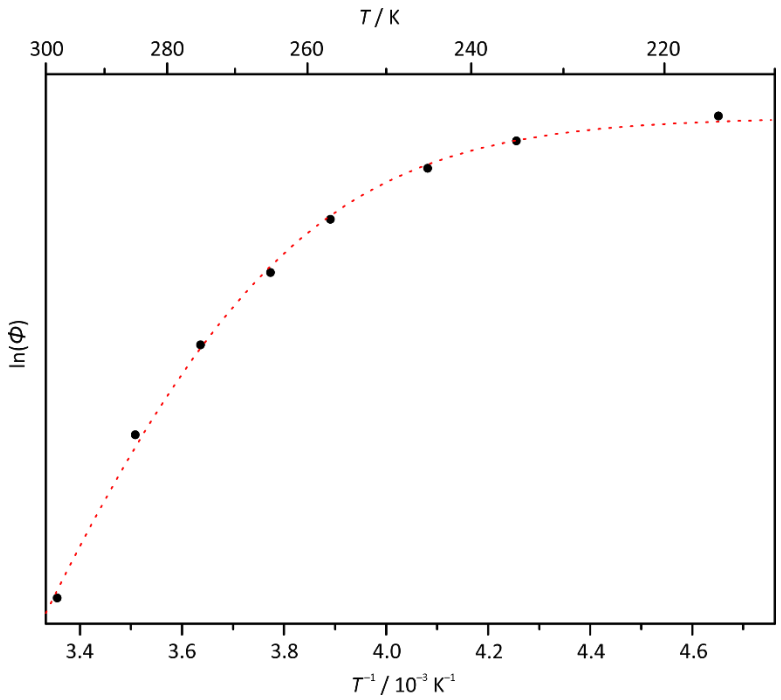

Figure S23 Variable-temperature emission plot ln(ϕ) vs. T^{-1} of $[Ru(bpy)_3](PF_6)_2$ in air-equilibrated butyronitrile in the temperature range between 300 K and 200 K. Activation barrier ΔE of 36.0 kJ mol^{-1} has been determined from the fit using Meyer's equation (literature value of ΔE = 42.6 kJ mol^{-1} for degassed butyronitrile).[3]

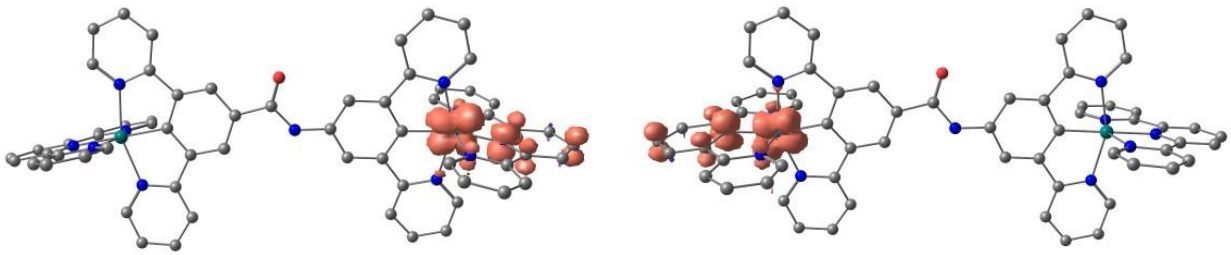

(0 kJ mol^{-1}) (6.3 kJ mol^{-1})

Figure S24 DFT calculated spin densities of the ^{3}MLCT states of $\mathbf{6}^{2+}$ (B3LYP, def2-SV(P), ZORA, COSMO(acetonitrile); contour value: 0.01). The relative electronic energies are given in parentheses.

[3] B. Durham, J. V. Caspar, J. K. Nagle and T. J. Meyer, *J. Am. Chem. Soc.*, 1982, **104**, 4803–4810.

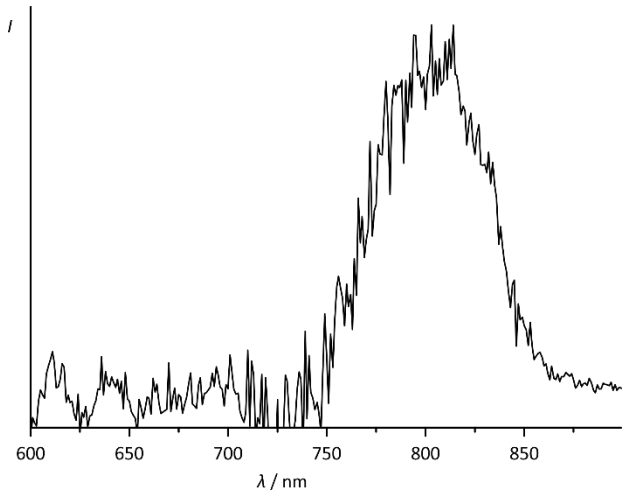

Figure S25 Difference of the emission spectra of **6**$^{2+}$ at 155 K in butyronitrile solution upon excitation at 560 nm and 480 nm.

Derivation of the equation used to fit the $\ln(\phi)$ vs. T^{-1} plots

Excited state reaction pathways:

$^1\mathrm{GS} \rightarrow {}^1\mathrm{MLCT}$	*Excitation*
$^1\mathrm{MLCT} \xrightarrow{\phi\sim 1} {}^3\mathrm{MLCT}$	*Intersystem crossing*
$^3\mathrm{MLCT} \xrightarrow{k_{\mathrm{nr}}} {}^1\mathrm{GS}$	*Direct non-radiative deactivation*
$^3\mathrm{MLCT} \xrightarrow{k_{\mathrm{r}}} {}^1\mathrm{GS}$	*Phosphorescence* $k_{nr} + k_r = k_1$
$^3\mathrm{MLCT} \underset{k_{-2}}{\overset{k_2}{\rightleftharpoons}} {}^3\mathrm{MC}$	*^{3}MLCT–^{3}MC surface crossing*
$^3\mathrm{MC} \xrightarrow{k_3} {}^1\mathrm{GS}$	*^{3}MC deactivation pathways*
$^3\mathrm{MC} \xrightarrow{k_4}$ photo products	
$^3\mathrm{MLCT} \underset{k_{-5}}{\overset{k_5}{\rightleftharpoons}} {}^3\mathrm{LL'CT}$	*^{3}MLCT–^{3}LL'CT surface crossing* $K_{LL'CT/MLCT} = \frac{k_5}{k_{-5}}$
$^3\mathrm{LL'CT} \xrightarrow{k_6} {}^1\mathrm{GS}$	*^{3}LL'CT deactivation*

We assume that the 3LL'CT state is chemically stable.

Based on the above reactions, the lifetime τ_0 of the ^{3}MLCT state can be expressed as follows:

$$\frac{1}{\tau_0} = k_1 + k_2\left(\frac{k_3+k_4}{k_{-2}+k_3+k_4}\right) + k_5\left(\frac{k_6}{k_{-5}+k_6}\right) \qquad (1)$$

In principle, all rate constants have to be considered as temperature-dependent. However, Meyer[4] argued, that the rate constants k_1 and k_3 for intersystem crossing describe processes at the respective Franck-Condon point and therefore are independent from the temperature. For the same reason, k_6 can be considered temperature-independent.

Following Meyer's argumentation, the back reaction from the ^{3}MC state to the ^{3}MLCT state is slow compared to the ^{3}MC state deactivation ($k_{-2} \ll k_3 + k_4$). Therefore, the first fraction $\left(\frac{k_3+k_4}{k_{-2}+k_3+k_4}\right)$ of equation (1) equals 1:

---

[4] B. Durham, J. V. Caspar, J. K. Nagle and T. J. Meyer, *J. Am. Chem. Soc.*, 1982, **104**, 4803–4810.

$$\frac{1}{\tau_0(T)} = k_1 + k_2(T) + k_5\left(\frac{k_6}{k_{-5}+k_6}\right) \quad (2)$$

According to Meyer, $k_2(T)$ is composed of a rate constant at infinite temperature (k_2^0) and an Arrhenius-like activation barrier term, taking the ^{3}MLCT–^{3}MC activation barrier $\Delta G_1^{\ddagger}$ into account.

$$k_2(T) = k_2^0 \exp\left(-\frac{\Delta G_1^{\ddagger}}{RT}\right) \quad (3)$$

For the second fraction $k_5\left(\frac{k_6}{k_{-5}+k_6}\right)$, a differentiation into two limiting cases is necessary:

a) When k_{-5} is small compared to k_6, the surface crossing to the ^{3}LL'CT state is irreversible and for the lifetime of the ^{3}MLCT state follows:

$$\frac{1}{\tau_0(T)} = k_1 + k_2(T) + k_5(T) \quad (4)$$

In this case, just as above for $k_2(T)$, $k_5(T)$ is composed of a rate constant at infinite temperature and an Arrhenius term, associated with the ^{3}MLCT-^{3}LL'CT activation barrier $\Delta G_2^{\ddagger}$.

$$k_5(T) = k_5^0 \exp\left(-\frac{\Delta G_2^{\ddagger}}{RT}\right) \quad (5)$$

b) When the back reaction from the ^{3}LL'CT to the ^{3}MLCT state is faster than the depopulation of the ^{3}LL'CT state into the ground state ($k_{-5} < k_6$), the ^{3}LL'CT and ^{3}MLCT states are in thermal equilibrium:

$$\frac{1}{\tau_0(T)} = k_1 + k_2(T) + K_{LL'CT/MLCT} \cdot k_6 \quad (6)$$

An exponential term is required to describe the temperature dependence of the last component of the equation in this case as well, but it contains the difference between the Gibbs free enthalpies of the ^{3}LL'CT and ^{3}MLCT states.

$$K_{LL'CT/MLCT} \cdot k_6 = k_6 \exp\left(-\frac{\Delta G^0}{RT}\right) \text{ with } \Delta G^0 = G^0_{LL'CT} - G^0_{MLCT} \quad (7)$$

Thus, the mathematical description with a sum over two exponential terms, which was used to fit the $\ln(\phi)$ vs. T^{-1} plots, is identical for both limiting cases, although the physical implications differ substantially:

a) $$\frac{1}{\tau_0(T)} = k_1 + k_2^0 \exp\left(-\frac{\Delta G_1^{\ddagger}}{RT}\right) + k_5^0 \exp\left(-\frac{\Delta G_2^{\ddagger}}{RT}\right) \quad (8a)$$

b) $$\frac{1}{\tau_0(T)} = k_1 + k_2^0 \exp\left(-\frac{\Delta G_1^{\ddagger}}{RT}\right) + k_6 \exp\left(-\frac{\Delta G^0}{RT}\right) \quad (8b)$$

A decision between the two cases a) or b) can only be made based on experimental data. When ΔG^0, the difference between the Gibbs free enthalpies of the ^{3}LL'CT and ^{3}MLCT states, is

negative, a decrease of the ^{3}MLCT lifetime $\tau_0(T)$ with decreasing temperature is expected for case b), while for case a) the lifetime should increase. In this study, the quantum yield $\phi(T)$ instead of the ^{3}MLCT lifetime $\tau_0(T)$ is measured. This, however, does not affect the obtained data neither qualitatively nor quantitatively, because ϕ and $\tau_0(T)$ are linearly related when k_r is independent from the temperature: $\phi(T) = k_r \cdot \tau_0(T)$. This temperature-independence of k_r has been observed in all studies on luminescent polypyridine ruthenium(II) complexes.